Altered photoreceptor metabolism in mouse causes late stage age-related macular degeneration-like pathologies

Shun-Yun Cheng[a], Joris Cipi[a], Shan Ma[a], Brian P. Hafler[b,c], Rahul N. Kanadia[d], Richard S. Brush[e,f,g,h], Martin-Paul Agbaga[e,f,g,h,1], and Claudio Punzo[a,1]

[a]Department of Ophthalmology and Visual Sciences, University of Massachusetts Medical School, Worcester, MA 01655; [b]Department of Ophthalmology and Visual Science, Yale School of Medicine, New Haven, CT 06510; [c]Department of Pathology, Yale School of Medicine, New Haven, CT 06510; [d]Department of Physiology and Neurobiology, University of Connecticut, Storrs, CT 06269; [e]Department of Cell Biology, University of Oklahoma Health Sciences Center, Oklahoma City, OK 73104; [f]Department of Ophthalmology, University of Oklahoma Health Sciences Center, Oklahoma City, OK 73104; [g]Harold Hamm Diabetes Center, University of Oklahoma Health Sciences Center, Oklahoma City, OK 73104; and [h]Dean A. McGee Eye Institute, University of Oklahoma Health Sciences Center, Oklahoma City, OK 73104

Age-related macular degeneration (AMD) is the leading cause of blindness in the elderly. While the histopathology of the different disease stages is well characterized, the cause underlying the progression, from the early drusen stage to the advanced macular degeneration stage that leads to blindness, remains unknown. Here, we show that photoreceptors (PRs) of diseased individuals display increased expression of two key glycolytic genes, suggestive of a glucose shortage during disease. Mimicking aspects of this metabolic profile in PRs of wild-type mice by activation of the mammalian target of rapamycin complex 1 (mTORC1) caused early drusen-like pathologies, as well as advanced AMD-like pathologies. Mice with activated mTORC1 in PRs also displayed other early disease features, such as a delay in photoreceptor outer segment (POS) clearance and accumulation of lipofuscin in the retinal-pigmented epithelium (RPE) and of lipoproteins at the Bruch's membrane (BrM), as well as changes in complement accumulation. Interestingly, formation of drusen-like deposits was dependent on activation of mTORC1 in cones. Both major types of advanced AMD pathologies, including geographic atrophy (GA) and neovascular pathologies, were also seen. Finally, activated mTORC1 in PRs resulted in a threefold reduction in di-docosahexaenoic acid (DHA)–containing phospholipid species. Feeding mice a DHA-enriched diet alleviated most pathologies. The data recapitulate many aspects of the human disease, suggesting that metabolic adaptations in photoreceptors could contribute to disease progression in AMD. Identifying the changes downstream of mTORC1 that lead to advanced pathologies in mouse might present new opportunities to study the role of PRs in AMD pathogenesis.

AMD | photoreceptors | geographic atrophy | wet AMD | photoreceptor metabolism

Age-related macular degeneration (AMD) is the leading cause of irreversible vision loss in the elderly (1, 2). Early disease stages are defined by the formation of drusen, which are lipid-rich deposits located between the retinal-pigmented epithelium (RPE) and the underlying Bruch's membrane (BrM) (1). Advanced disease stages are characterized by confluent RPE atrophy, referred to as geographic atrophy (GA), and/or edemas that result from choroidal and/or retinal neovascularization (1). Both advanced stages cause blindness through extensive secondary loss of photoreceptors (PRs). Notably, 20% of individuals with early stage drusen progress to the advanced disease forms. Although the RPE is the primary cell type affected in advanced AMD, what causes disease progression remains unclear (2).

Two factors that contribute to drusen genesis and disease progression in AMD are genetic variations in genes of the innate immune system and poor diet (3–7). Dysregulation of complement components such as C3 and CFH, which are central to the activation and inhibition of the complement system, respectively, is thought to contribute to RPE atrophy (3). Excessive consumption of saturated dietary fats also influences drusen formation as drusen are rich in lipoproteins that are partially derived from the circulation (8). In contrast, foods enriched in polyunsaturated fatty acids, such as the omega-3 fatty acid docosahexaenoic acid (DHA), have been linked through many epidemiological studies to a risk reduction for advanced AMD (9, 10). Although DHA is highly enriched in photoreceptor outer segments (POSs), the mechanism of protection remains unknown (11).

The role of PRs in disease pathogenesis remains to be determined as PRs have been associated with both the early and late disease stages (8, 12–14). For example, macular translocation procedures revealed that PRs can cause the late disease stage of GA. Patients whose retina was rotated to move macular cones away from an area of GA to an area of healthy RPE redeveloped GA where the cones were translocated (12, 13). Similarly, analyses on the distribution of soft drusen and subretinal drusen deposits revealed that their preferential location mirrors the density of

Significance

The main cause for blindness in the elderly worldwide is age-related macular degeneration (AMD). What causes AMD remains unknown. The high metabolic demands of photoreceptors are thought to contribute to disease pathogenesis, yet whether photoreceptor metabolism differs in individuals with AMD has not been determined. Here, we show that photoreceptor metabolism does differ between diseased and non-diseased individuals. Mimicking the metabolic profile of diseased individuals in mouse resulted in the similar advanced pathologies as those that cause blindness in humans. A disease model with photoreceptors as a contributing factor explains also why AMD affects preferentially the macula; it is the region of highest photoreceptor density. The data might open new avenues to study the role of PRs in disease pathogenesis.

cones and rods, respectively (8, 14). In both cases, the high and differential metabolic demands of cones and rods are thought to contribute to disease pathogenesis (8, 12–14). However, whether the metabolic demands of PRs differ in individuals with AMD has not been investigated. This question is particularly pertinent since glucose shortage in PRs of AMD patients has been predicted by several models of disease pathogenesis. For example, the mitochondrial dysfunction seen in RPE cells of AMD patients has been proposed to reduce glucose transfer from the RPE to PRs. The idea here is that, to compensate for the energy shortfall caused by dysfunctional mitochondria, the RPE starts utilizing glucose itself, rather than providing it to PRs and use PR-derived lactate (15). The finding of a lipid wall at the BrM that forms during the early drusen stage of the disease (oil spill model) is also predicted to cause a glucose shortage in PRs as this hydrophobic barrier should reduce the transfer of hydrophilic molecules like glucose from the choroidal vascular to the RPE and thus PRs (8). These models are not mutually exclusive; rather they represent sequential disease stages that once superimposed could compound the glucose shortage in PRs even more. Thus, if these models are correct, one would expect to find adaptive changes in PRs of AMD patients that allow PRs to cope with a glucose shortfall.

Here, we show that the expression of two genes that are characteristic of PR metabolism and cell growth (16–20), namely pyruvate kinase muscle isozyme M2 (*Pkm2*) and hexokinase-2 (*Hk2*), is increased in individuals with AMD. HK2 improves glucose retention and PKM2 allows for a more efficient diversion of glycolytic intermediates into the pentose phosphate pathway (PPP). Because the PPP promotes cellular NADPH synthesis and NADPH is a reducing agent that is also required for fatty acid synthesis, the PPP helps reduce cellular oxidative stress and maintain the renewal of the lipid-rich POSs (16, 17, 19). HK2 and PKM2 have both been implicated during secondary cone death in retinitis pigmentosa where cone death was found to be in part due to a glucose shortage in cones (18, 21, 22). One of the adaptive responses of cones in retinitis pigmentosa is to increase the expression of these two proteins through increased activity of the mammalian target of rapamycin complex 1 (mTORC1), a key regulator of cell metabolism and cell growth (22–25). Loss of mTORC1 activity or HK2 accelerates cone death in retinitis pigmentosa while constitutive activation of mTORC1 promotes cone survival (18, 22). Similarly, loss of mTORC1 activity in the sodium iodate model of GA accelerates PR death (26). Therefore, to mimic the adaptive responses seen in PRs of AMD patients and study their effect on retinal and RPE health, we generated a mouse model with constitutive activation mTORC1 in PRs of wild-type mice. This was achieved by deletion of the tuberous sclerosis complex 1 (*Tsc1*) gene, a negative regulator of mTORC1 (27). We found an age- and mTORC1-dependent onset of advanced AMD pathologies, including GA and neovascular pathologies, at a frequency similar to that seen in humans (2). Mice with activated mTORC1 also displayed early disease features, such as accumulation of lipoproteins at the BrM (8, 14) and changes in complement C3 and CFH deposition (3). These changes occurred uniformly across the tissue independent of the presence of any advanced pathology. Finally, we also found a reduction in 1,2-docosahexanoyl-sn-glycero-3-phospholipid species in retinas of these mice. Feeding mice a DHA-enriched diet alleviated most pathologies (9, 10). The data mimic most aspects of the human disease, suggesting that metabolic adaptations in PRs could be a contributing factor for disease progression in AMD.

Results

HK2 and PKM2 Expression Are Increased in PRs of AMD Patients.
HK2 and PKM2 are two glycolysis enzymes that are generally associated with cell growth during development, as well as tumorigenesis, as they promote progrowth pathways such as the PPP (28, 29). While normally not expressed in most postmitotic neurons, both genes are a key signature of PR metabolism (16–20). This is because PRs are in a constant phase of cell growth, due to the need to replace the daily shed POSs. Both genes thus play an important role in POS renewal, function, and survival, in particular under nutrient stress (16–22). To determine whether PR metabolism differs in individuals with AMD, we analyzed the expression of these two key metabolic genes in human donor eyes with or without AMD. On retinal sections, we found increased expression of PKM2 and HK2 in PRs of AMD patients (*n* = 3), with the highest increase found in cones (Fig. 1*A* and *SI Appendix*, Fig. S1 *A* and *B*). Interestingly, expression in nondiseased retinas was quite low for PKM2 as those sections required up to five times longer exposure to the histochemical reagent in order for a strong signal to emerge (Fig. 1*A*). To allow for a more linear comparison between samples, we repeated the experiments using immunofluorescence (*SI Appendix*, Fig. S1*A*). A twofold scaling of the signal between nondiseased and diseased tissue was sufficient to reveal a PR signal in nondiseased tissue without causing overexposure of the signal in diseased retinas. Interestingly, the expression of both genes in mouse has been shown to decline with age (*SI Appendix*, Fig. S1*C*) (18, 30). This could in part account for the stark difference in signal intensity seen between diseased and nondiseased individuals. In summary, the data show that levels of HK2 and PKM2 increase in PRs of individuals with AMD, suggesting that glucose availability is reduced in diseased individuals.

*rod*Tsc1$^{-/-}$ Mice Develop Advanced AMD Pathologies.
We previously showed that nutrient-deprived cones have higher mTORC1 activity and that further activation of mTORC1 promotes the survival of nutrient-deprived cones in part through increased expression HK2 and PKM2 (21, 22, 26). To determine the effect of such metabolic changes on retinal and RPE health in wild-type mice, we constitutively activated mTORC1 in rods by deletion of the *Tsc1* gene (henceforth referred to as *rod*Tsc1$^{-/-}$) using the *Cre-lox* system (31). Increased mTORC1 activity was confirmed by immunofluorescence and Western blot analyses for phosphorylated ribosomal protein S6 (p-S6) (Fig. 1 *B* and *C*) (24). Similarly, changes in PR metabolism were confirmed by quantifying retinal PKM2, lactate, and NADPH levels (Fig. 1 *C–E*).

To determine whether *rod*Tsc1$^{-/-}$ mice develop advanced AMD-like pathologies, we followed the mice over a period of 18 mo (18M) by funduscopy and fluorescein angiography (Fig. 2 and *SI Appendix*, Fig. S2). We found, at 2M, migration and accumulation of microglia into the subretinal space and, at 4M, formation of retinal folds, some of which were filled with microglia (*SI Appendix*, Fig. S3) (32). Flat mount and section analyses revealed highly autofluorescent RPE cells opposing these folds (Fig. 3 *A* and *B*), which in mice may be a direct consequence of acutely compromised or lost RPE cells (33, 34).

GA was seen in 5% of mice at 6M and 25% of mice at 18M (Fig. 2*C*). Interestingly, while GA did also overlap with areas of retinal folds, the presence of these folds was not required for GA to develop. Generally, pathologies worsened within the same animal with age (*SI Appendix*, Fig. S2). To confirm that areas of GA correlate with regional PR atrophy and that RPE atrophy precedes PR atrophy, we compared the RPE and corresponding retina by flat mount analyses (Fig. 3 *A–C*), identified intermediate RPE pathologies (Fig. 3*D*), and performed semithin sectioning through regions of GA that were identified by optical coherence tomography (OCT) (Fig 3 *E* and *F*).

Neovascular pathologies reaching a frequency of 7% by 18M were seen less frequently than GA (Fig. 2*C*) although most coincided with regions of GA. While we readily detected retinal neovascular pathologies on semithin sections (Fig. 3*F*), choroidal neovascular pathologies were not evident on RPE flat mounts. However, given the overall low frequency of neovascular pathologies, we cannot conclude that choroidal neovascular pathologies do not occur. Except for the accumulation of subretinal
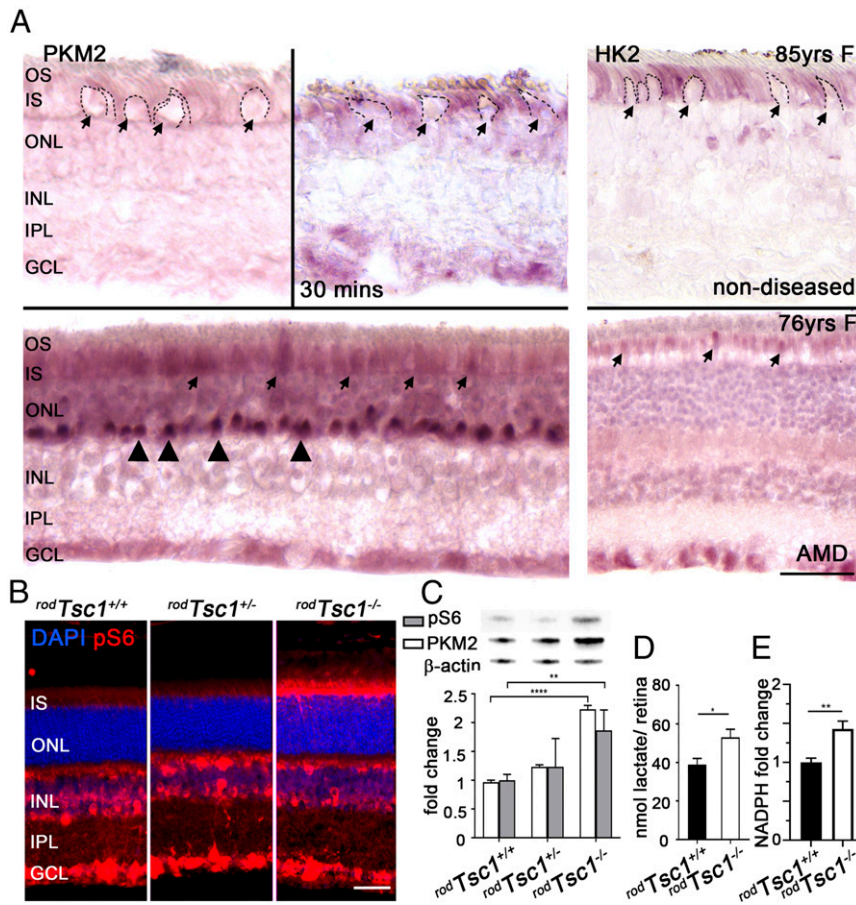
Fig. 1. Expression levels of PKM2 and HK2 are increased PRs of AMD patients. (*A*) Immunohistochemistry (IHC) showing increased expression of PKM2 and HK2 (purple) on retinal cross-sections. Increased expression is seen throughout the PR layer of AMD patients and particularly in cone inner segments (arrows) and cone pedicles (arrowheads). Dotted lines demark some of the cone inner segments in nondiseased individuals. Enzymatic reaction for IHC was 6 min, except for the second panel of a nondiseased individual with the PKM2 antibody (30 min.; all diseased sections and all nondiseased sections in *A* are from the same retina, respectively; F: female of age indicated in years). (Scale bar: 45 μm.) (*B*) Immunofluorescence for p-S6 in 2M-old mice of genotypes indicated (red; blue nuclear DAPI). (Scale bar: 50 μm.) (*A* and *B*) GCL, ganglion cell layer; INL, inner nuclear layer; IPL, inner plexiform layer; IS, inner segments; ONL, outer nuclear layer; OS, outer segments. (*C*) Quantification of Western blots for p-S6 and PKM2 with retinas from 2M-old mice ($n = 3$) of genotypes indicated. On *Top* are representative Western images for each protein plus the actin control Western. Results are shown as mean ± SEM (**$P < 0.01$, ****$P < 0.0001$). (*D* and *E*) Measurements of retinal lactate (*D*) and NADPH (*E*) levels at 2M of genotypes indicated ($n = 4$ for lactate and $n = 8$ for NADPH). Results are shown as mean ± SEM (*$P < 0.05$, **$P < 0.01$).

microglia, none of the heterozygous $^{rod}Tsc1^{+/-}$ mice nor any of the Cre^- littermate control mice ($^{rod}Tsc1^{+/+}$) developed advanced pathologies (Fig. 2 *B* and *C*). Consistent with this, activation of mTORC1 and the increase in PKM2 expression levels were both minimal in $^{rod}Tsc1^{+/-}$ mice (Fig. 1*C*).

To determine if RPE stress and atrophy also occurred outside regions of GA, we determined the percentage of polynucleated RPE cells and measured changes in RPE cell size in non-GA areas. At 18M, we found a significant increase in polynucleated and enucleated as well as hypertrophic RPE cells (Fig. 3*G*). The data indicate that loss of *Tsc1* in rods contributes to a widespread RPE pathology that precipitates to regional GA in some animals. We therefore determined if overall PR survival and function were perturbed. Consistent with a widespread RPE pathology, we found a small decrease in the thickness of the PR layer at 18M (*SI Appendix*, Fig. S4*A*). This decrease may also explain the less prominent appearance of retinal folds with age (*SI Appendix*, Fig. S2) as they begin to flatten with the loss of PRs. Interestingly, rod a-wave amplitudes were higher in $^{rod}Tsc1^{-/-}$ mice at early time points but declined to the littermate control amplitudes by 18M (*SI Appendix*, Fig. S4*B*). The early higher amplitude is in line with our previous findings where loss of HK2

leads to a reduction of the scotopic response and a reduction in retinal lactate and NADPH levels (18). Thus, the early higher amplitude may reflect higher energy availability. Alternatively, increased transcription or translation of phototransduction genes due to increased PKM2 expression or increased mTORC1 activity, respectively, could also account for higher a-wave amplitudes in $^{rod}Tsc1^{-/-}$ mice (16, 24). Further studies are warranted to determine what specifically causes these higher a-wave amplitudes in $^{rod}Tsc1^{-/-}$ mice. Interestingly, c-wave amplitudes, which reflect in part RPE health, did not differ between $^{rod}Tsc1^{-/-}$ mice and controls (*SI Appendix*, Fig. S4*D*) (20). Here, higher retinal lactate levels may have benefited a sick RPE (15, 20). Overall, the data indicates that loss of *Tsc1* in rods leads to a slow progressive disease, except for areas where advanced pathologies precipitate.

To confirm that GA was not caused by aberrant CRE recombinase expression in the RPE, we stained RPE flat mounts for p-S6. While occasional p-S6 positive cells were seen in both $^{rod}Tsc1^{-/-}$ mice and controls at 2M (*SI Appendix*, Fig. S5*A*), we did not find CRE recombinase expression in p-S6–positive cells (*SI Appendix*, Fig. S5*B*). Additionally, the number of p-S6–positive cells increased dramatically with age (*SI Appendix*, Fig. S5 *A* and *C*). This increase likely reflects an increase in the number of sick
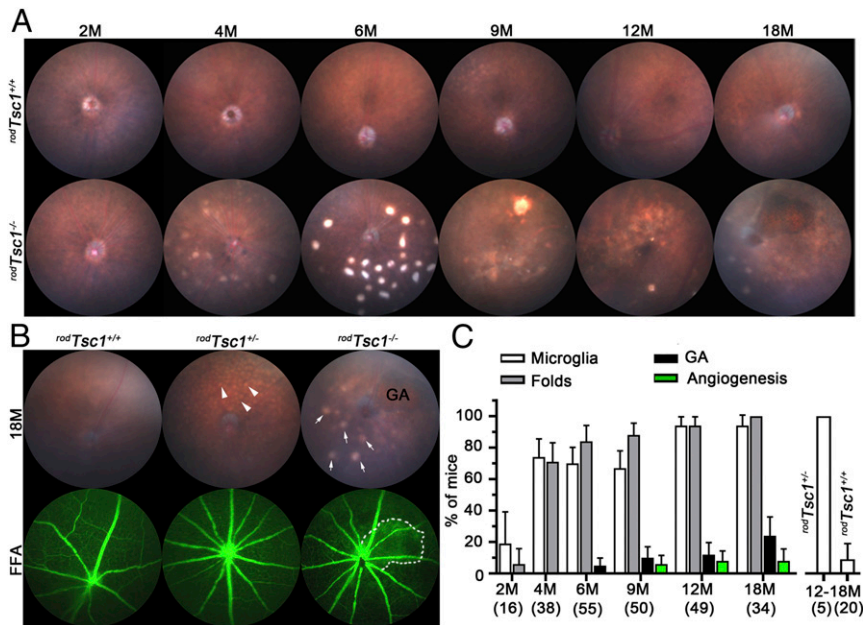
Cheng et al.

Fig. 2. Aged $^{rod}Tsc1^{-/-}$ mice develop GA and neovascular pathologies. (*A*) Representative fundus images of littermate controls (*Top Row*) and $^{rod}Tsc1^{-/-}$ mice (*Bottom Row*) at ages indicated. (*B*) Representative fundus fluorescein angiography (FFA) (*Bottom Row*) images with corresponding fundus image (*Top Row*) at 18M of genotypes indicated. $^{rod}Tsc1^{+/+}$ mice show occasionally some microglia accumulation while all $^{rod}Tsc1^{+/-}$ mice show microglia accumulation (arrowheads). $^{rod}Tsc1^{-/-}$ mice develop retinal folds (arrows), GA (as indicated), and neovascular pathologies (dotted line). (*C*) Percentage distribution of phenotypes explained in *B* in $^{rod}Tsc1^{-/-}$ mice at indicated ages. The last two bars show control mice where only microglia accumulation is seen. Bars show percentage ± margin of error (M.O.E.). Numbers in parentheses: number of mice analyzed (M, months).

RPE cells in $^{rod}Tsc1^{-/-}$ mice as increased mTORC1 activity in the RPE has been associated with RPE dysfunction, senescence, and cell loss (35–37). Moreover, a recent study that deleted *Tsc1* from all RPE cells did not report any advanced AMD pathologies (37).

$^{rod}Tsc1^{-/-}$ Mice Also Display Early Disease Features. The metabolic demands of PRs have been proposed to contribute to lipoprotein accumulation and drusen formation (8). To determine if the metabolic changes induced in PRs also contribute to lipoprotein accumulation, we analyzed the distribution of ApoB and ApoE at the BrM. We found accumulation of both lipoproteins at the RPE basal lamina and BrM, independent of any advanced pathology (*SI Appendix*, Fig. S6*A*). Electron microscopy (EM) analyses revealed neutral lipids within the BrM, as well as basal laminar deposits and thickened BrM in areas of GA (*SI Appendix*, Fig. S6*B*). However, drusen-like deposits were not seen; rather, basal mounds were quite common (*SI Appendix*, Fig. S6*C*). Additionally, we found increased autofluorescence in the RPE of $^{rod}Tsc1^{-/-}$ mice, indicative of increased lipofuscin accumulation (*SI Appendix*, Fig. S6*D*).

The complement system plays an important role in AMD pathogenesis (3). In particular, C3 activation is thought to contribute to RPE atrophy and GA (3). We found a uniform downregulation of C3 at the BrM and a uniform up-regulation of CFH in $^{rod}Tsc1^{-/-}$ mice (*SI Appendix*, Fig. S6*A*). In all, the findings show that these early disease features, which are induced by activation of mTORC1 in rods, occur uniformly across the tissue independent of the presence of any advanced pathology.

AMD-Like Pathologies Are Dependent on the Dose of Activated mTORC1. To test the requirement of mTORC1 to the pathologies seen, we generated mice with simultaneous deletion of *Tsc1* and the mTORC1 adaptor protein Raptor (referred to $^{rod}Tsc1^{-/-}$ $^{rod}Raptor^{-/-}$ mice). Fundus imaging reveled no pathology, except for the accumulation of microglia in 76% of mice aged between

12M and 18M (Fig. 4 *A* and *B*). Even heterozygous *Raptor* mice ($^{rod}Tsc1^{-/-}$ $^{rod}Raptor^{+/-}$) did not develop any GA or neovascular pathologies by 12M (Fig. 4*B*). However, retinal folds were present, albeit at lower frequency. The absence of any severe pathology was in line with the quantification of polynucleated RPE cells and RPE cell size, which revealed no substantial difference among these lines at 12M (Fig. 4*C*). Western blot analyses for p-S6 and PKM2 confirmed the reduction in mTORC1 activity (Fig. 4*E*). Interestingly, while p-S6 levels in $^{rod}Tsc1^{-/-}$ $^{rod}Raptor^{+/-}$ showed a dose-dependent decline when compared to in $^{rod}Tsc1^{-/-}$ mice, PKM2 levels remained similar to PKM2 levels in $^{rod}Tsc1^{-/-}$ (compare Fig. 4*D* with Fig. 1*C*). In contrast, lactate and NADPH levels remained at the levels of *Cre*$^-$ controls in heterozygous $^{rod}Tsc1^{-/-}$ $^{rod}Raptor^{+/-}$ mice (Fig. 4 *E* and *F*). To determine to which extend this affected the early pathologies, we reanalyzed the accumulation of ApoB, ApoE, C3, and CFH. While accumulation of these markers was restored to normal in $^{rod}Tsc1^{-/-}$ $^{rod}Raptor^{-/-}$ mice, heterozygous $^{rod}Tsc1^{-/-}$ $^{rod}Raptor^{+/-}$ mice displayed a more intermediate phenotype (Fig. 4*G*). ApoB showed almost no accumulation while ApoE accumulation was similar to that seen in $^{rod}Tsc1^{-/-}$ mice. Similarly, CFH showed very little accumulation, and C3 was substantially reduced. The data suggest that the development of early and late pathologies is driven in a dose-dependent manner by increased mTORC1 activity. The extent to which alterations in the exchange of lactate and glucose between PRs and the RPE (20) contribute to advanced pathologies remains to be investigated.

RPE Phagocytosis Is Perturbed in $^{rod}Tsc1^{-/-}$ Mice. Impaired RPE lysosomal activity has been associated with AMD (38–40). The uniform nature of RPE cell stress led us to investigate if POS clearance was perturbed in the $^{rod}Tsc1^{-/-}$ mice. Since shedding of rod POSs is circadian, clearance can be monitored over time on RPE flat mounts stained for the rhodopsin protein. We found that rod POS clearance was already significantly slowed at 2M in
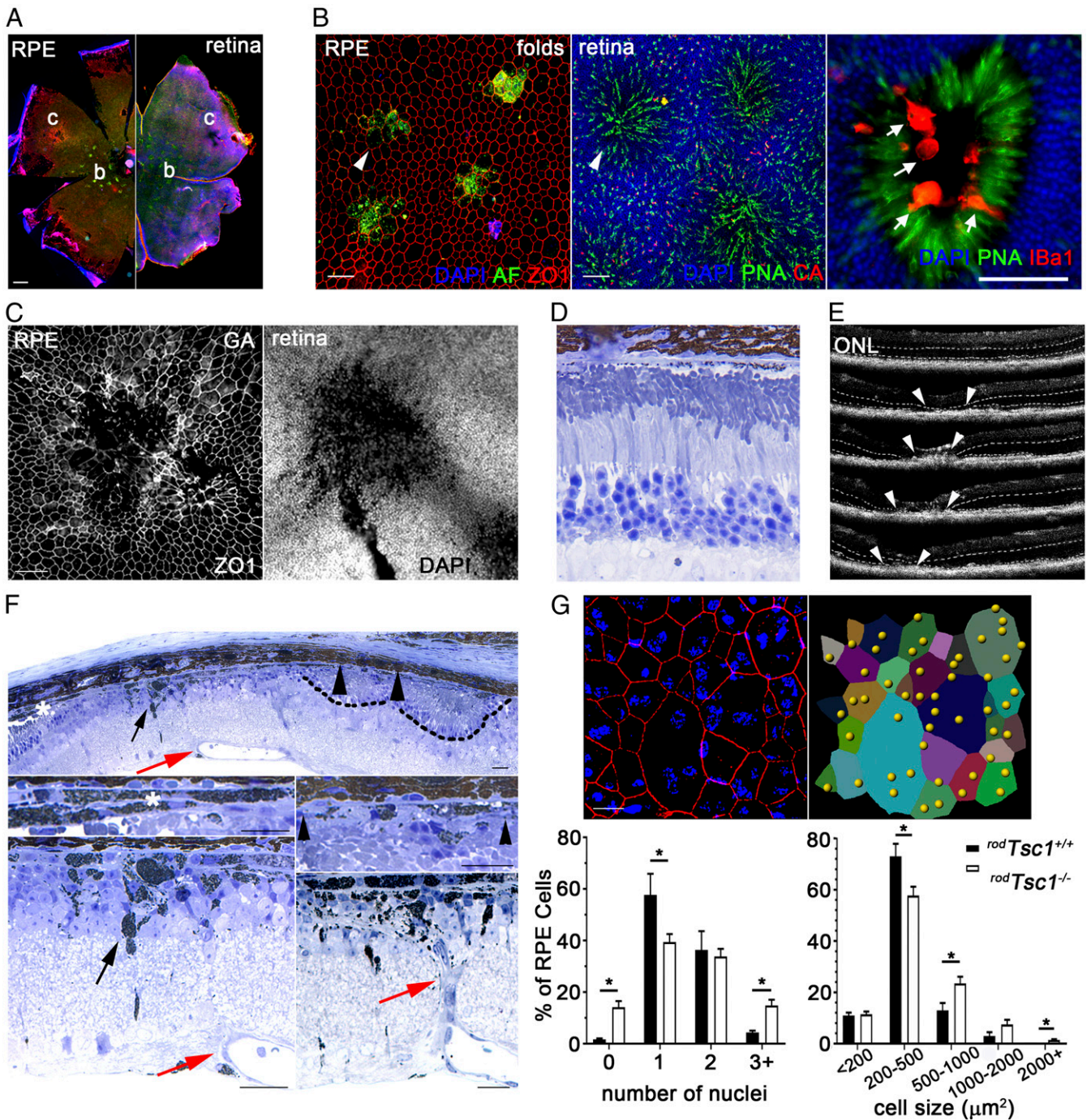
Fig. 3. Histological analyses of advanced AMD-like pathologies. (*A*) RPE and corresponding retinal flat mount of the same eye, showing autofluorescent RPE cells and the corresponding area with retinal folds marked with the letter b, and an area of GA and corresponding PR atrophy marked with the letter c. RPE whole mount is shown in the *Left Half*, and the corresponding retina in the *Right Half* of the panel. (Scale bar: 300 μm.) (*B*) Higher magnification of the region in *A* marked with letter b showing autofluorescent RPE cells (arrowhead: *Left*) that correspond to retinal folds (arrowhead: *Middle*). *Right* shows higher magnification of a fold (different eye) with Iba-1 staining (red) marking microglia (arrows). (Scale bars: 50 μm.) (*C*) Higher magnification of area of GA marked in *A* with the letter c showing in gray scales loss of RPE cells (*Left*) and retinal PRs (*Right*; PR side up showing reduced nuclear DAPI density). Note that no folds are visible in the are of GA in *A* (letter c), meaning that folds are not required for the formation of GA. (Scale bar: 50 μm.) Colors in *A–C* are as indicated by labels in panels. Annotation of colors for *A* is indicated in the first two images of *B* (blue, nuclear DAPI; green, autofluorescence [AF] or cone sheets marked by peanut agglutinin lectin [PNA]; red, RPE boundaries marked by ZO1, cones marked by cone arrestin [CA] or microglia marked by Iba-1). (*D*) Semithin section through intermediate stage of GA showing RPE atrophy with PRs still present. No fold is present in this area of RPE atrophy (image size: ~100 μm). (*E*) Consecutive OCT images through area of GA identified by fundus (same eye as shown in Fig. 2 *A* and *B*: 18M with GA), showing collapse (between arrowheads) of the outer nuclear layer (ONL) (between dotted lines). (*F*) Semithin sections of eye with GA shown in *E* showing multilayered RPE (white asterisk), RPE migration into the retinal proper (arrow), RPE atrophy (between arrowheads), and retinal angiogenesis (red arrows). As PRs die, retinal folds flatten if they overlap with areas of GA. Reminiscence of retinal folds is indicated by dotted lines. (Scale bars: 20 μm.) (*G*) RPE polynucleation and hypertrophy analyses. *Top* shows representative RPE image of cell boundaries marked by ZO1 (red signal) used for quantification analyses with output from the IMARIS software on the *Right* to identify cell shape, size, and nuclei (blue signal, nuclear DAPI). *Bottom* shows quantification of RPE polynucleation (*Left*) and distribution of RPE cell size (*Right*). Bars show mean ± SEM (*n* = 4 RPE flat mounts; *$P < 0.05$). (Scale bar, 10 μm.)
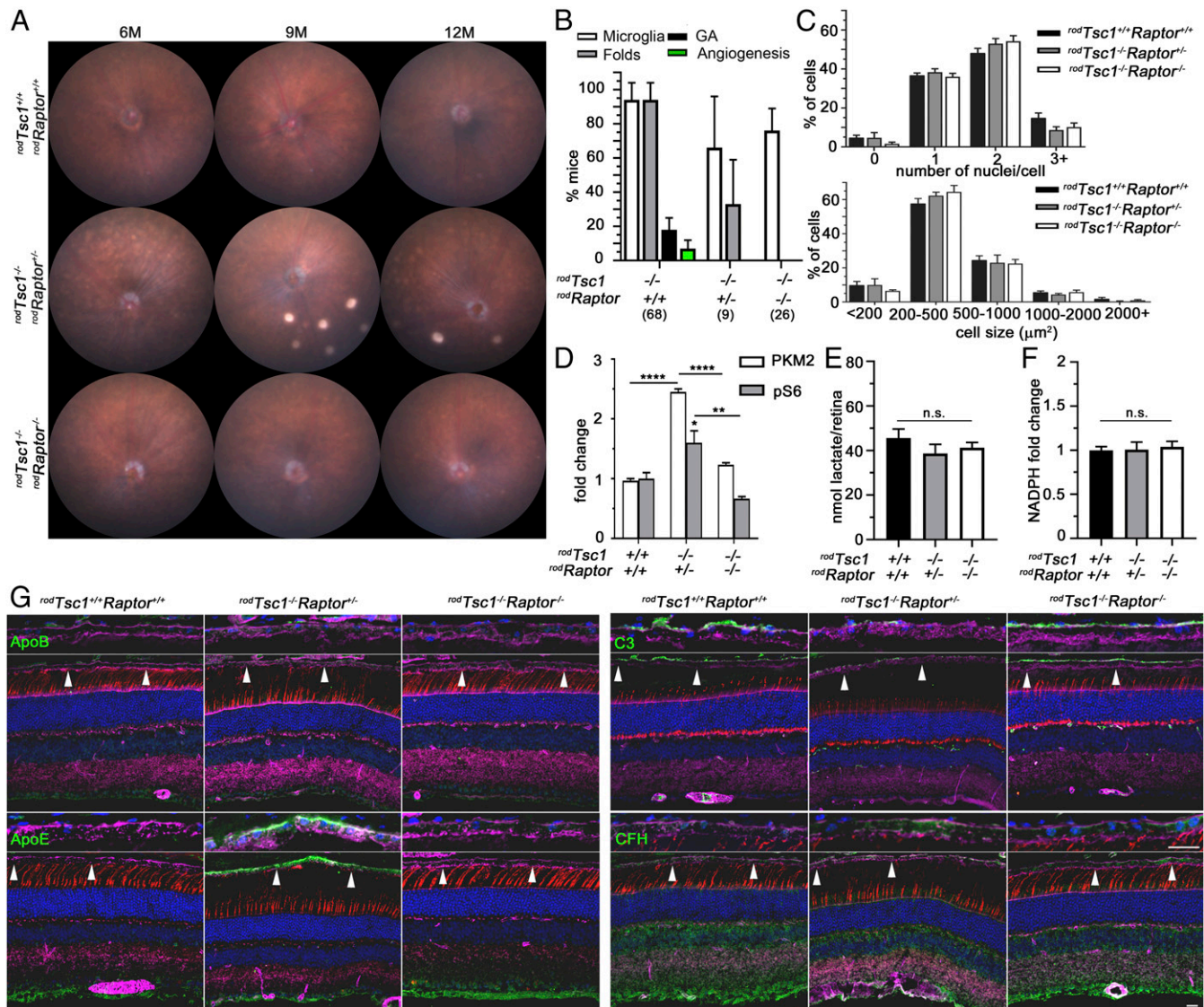
Fig. 4. AMD-like pathologies are dependent on the dose of activated mTORC1. (*A*) Representative littermate fundus images of $^{rod}Tsc1^{+/+}$ $^{rod}Raptor^{+/+}$ (*Top*), $^{rod}Tsc1^{-/-}$ $^{rod}Raptor^{+/-}$ (*Middle*), and $^{rod}Tsc1^{-/-}$ $^{rod}Raptor^{-/-}$ (*Bottom*) mice at ages indicated. Fundus of $^{rod}Tsc1^{-/-}$ are shown in Fig. 2 and *SI Appendix*, Fig. S2. (M, months). (*B*) Percentage distribution of retinal pathologies scored with mice between 12M and 18M of age of genotypes indicated. $^{rod}Tsc1^{+/+}$ are shown in Fig. 2*C*. The graph shows the percentage ± M.O.E. Numbers in parentheses, number of mice analyzed. (*C*) Analyses of RPE polynucleation and RPE hypertrophy at 12M of genotypes indicated. Bars show mean ± SEM (*n* = 4 mice). (*D*) Quantification of retinal PKM2 (white) and p-S6 (gray) levels performed by Western blot in 2M-old mice of genotypes indicated. Bars show mean ± SEM (*n* = 3 mice) (*$P < 0.05$, **$P < 0.01$, ****$P < 0.0001$). (*E* and *F*) Retinal lactate (*E*) and NADPH (*F*) levels at 2M of age of genotypes indicated. Bars show mean ± SEM (*n* = 4 for lactate and *n* = 7 for NADPH; n.s.: not significant). (*G*) Immunofluorescence for ApoB, ApoE, C3 and CFH (green signal) on retinal sections of 12M-old mice of genotypes indicated. Higher magnification of the region between arrowheads is shown on *Top* of each panel. Blue, nuclear DAPI; red, peanut agglutinin lectin to detect cone segment; magenta, ZO1 to visualize RPE in ApoE and C3 panels or Phalloidin to visualize RPE in ApoB and CFH panels. Images are representative of three independent experiments with three different animals. (Scale bars: 20 μm.)

$^{rod}Tsc1^{-/-}$ mice and was rescued in $^{rod}Tsc1^{-/-}$ $^{rod}Raptor^{-/-}$ mice, indicating that the effect was due to increased mTORC1 activity in rods (Fig. 5 *A–C*).

POSs are rich in lipids (11, 41), and mTORC1 is known to regulate lipid synthesis (24, 25). To determine a cause for the delayed POS clearance by the RPE, we profiled the retinal lipid composition of $^{rod}Tsc1^{-/-}$ mice. We found an approximately three-fold decrease in di-DHA (44:12) containing phosphatidylethanolamine (PE) and phosphatidylcholine (PC) lipids in total retinal (Fig. 5*D*) and POS preparations (Fig. 5*E*). To test if this drop in di-DHA PE and PC lipids contributes to the delay in POS clearance, we fed $^{rod}Tsc1^{-/-}$ mice a diet enriched with 2% DHA. The

2% value was based on a study that showed a beneficial effect with DHA supplementation on delaying disease progression in humans (42). Feeding $^{rod}Tsc1^{-/-}$ mice a 2% DHA-enriched diet from weaning onwards improved POS clearance at 2M (Fig. 5*F*). To test if delayed POS clearance can also be improved once the delay has occurred, we fed 6M-old $^{rod}Tsc1^{-/-}$ mice the DHA-enriched diet for 2 wk. This had an even more pronounced effect as POS clearance was more affected at 6M (Fig. 5*G*). To determine if dietary DHA also affected overall RPE health, we kept mice on the DHA diet from weaning onwards until 6M. This reduced the percentage of polynucleated RPE cells (Fig. 4*H*), improved fundus pathologies (Fig. 5*I*), prevented the accumulation of ApoB, ApoE,
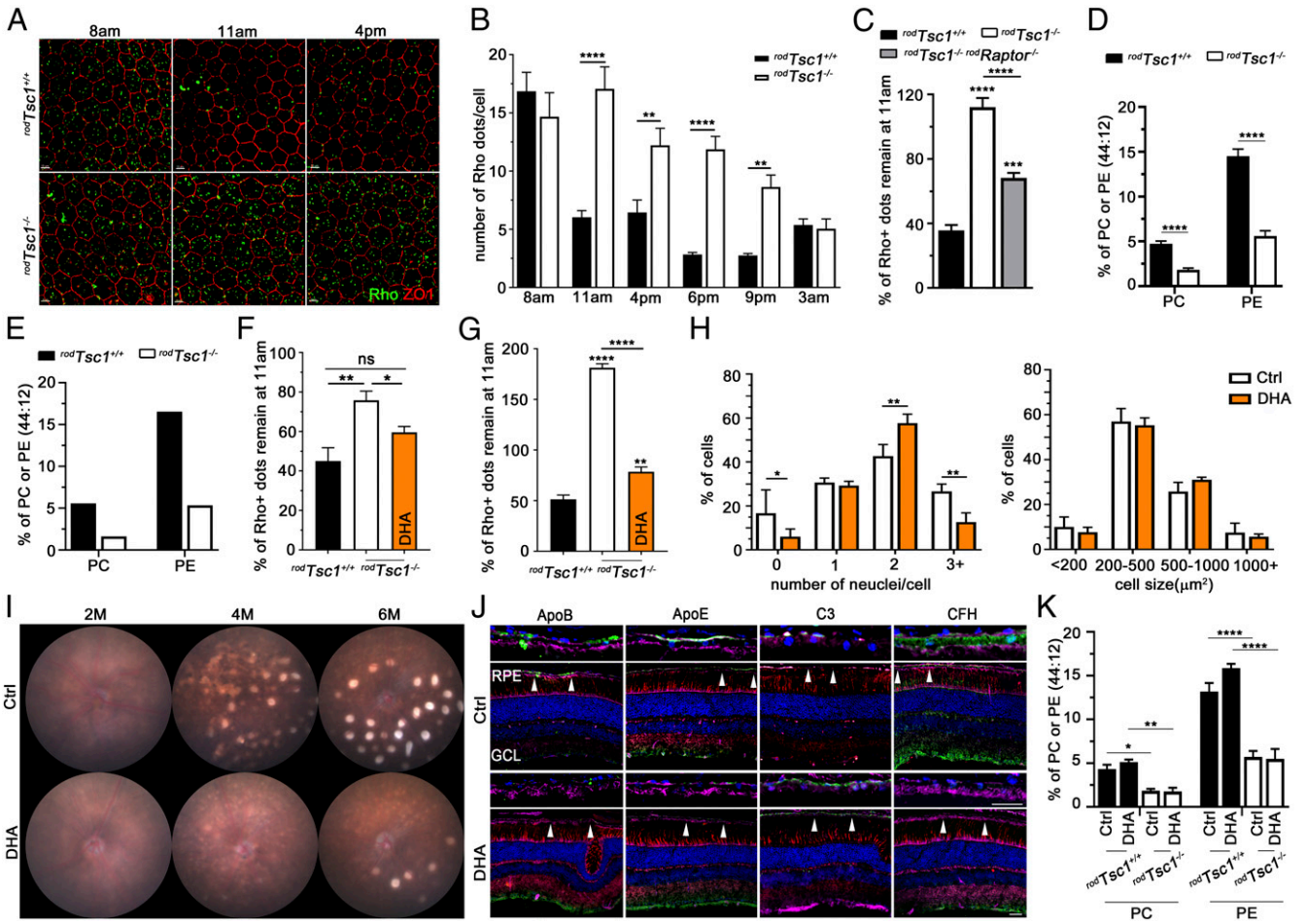
NEUROSCIENCE

Fig. 5. RPE digestion of POSs is perturbed in $^{rod}Tsc1^{-/-}$ mice. (*A*) Representative immunofluorescence images of RPE whole mounts from 2M-old $^{rod}Tsc1^{-/-}$ mice at time of day indicated showing delayed POS clearance by RPE cells (*Bottom Row*) when compared to control mice (*Top Row*). POSs are shown in green stained for RHODOPSIN while RPE cell boundaries are shown in red stained for ZO1 expression. (Scale bars: 10 μm.) (*B*) Quantification of the number of Rho-positive dots per RPE cell over the course of the day from 2M-old mice of genotypes indicated, obtained from immunofluorescence images as shown in *A*. Bars show mean ± SEM (*n* = 6–8 RPE flat mounts; **P < 0.01; ****P < 0.0001). (*C*) Delay of POS clearance shown as percentage of remaining dots 3 h after peak shedding (ratio between 11 AM and 8 AM) in 2M-old mice of genotypes indicated. Bars show mean ± SEM (*n* = 6–8 RPE flat mounts; ***P < 0.001; ****P < 0.0001). (*D*) Relative percentage of di-DHA PE (44:12) and PC (44:12) lipids from total retinal extracts of genotypes indicated at 2M. Bars show mean ± SEM (*n* = 6–9 mice, two retinas per mouse; ****P < 0.0001). (*E*) Same as in *D* with purified POSs pooled from six retinas per genotype. (*F*) POS clearance shown as percentage of remaining dots 3 h after peak shedding (ratio between 11 AM and 8 AM) in 2M-old mice that were fed a DHA or control diet between weaning to 2M. Shown are mean ± SEM (*n* = 6 RPE flat mounts; *P < 0.05; **P < 0.01; ns: not siginificant). (*G*) Same as in *F* with 6M-old mice that were fed a DHA diet for only 2 wk. Shown are mean ± SEM (*n* = 6 RPE flat mounts; **P < 0.01; ****P < 0.0001). (*H*) RPE polynucleation (*Left*) and hypertrophy (*Right*) analyses of $^{rod}Tsc1^{-/-}$ mice that were fed a DHA or control diet between weaning to 6M. Bars are mean ± SEM (*n* = 6 mice RPE flat mounts; *P < 0.05; **P < 0.01). (*I*) Representative fundus images of $^{rod}Tsc1^{-/-}$ mice on control (*Top Row*) or DHA (*Bottom Row*) diet from weaning onwards until time point indicated in panel (M, months). (*J*) AMD-related markers on retinal sections of $^{rod}Tsc1^{-/-}$ mice that were fed a DHA or control diet between weaning to 6M. Proteins of interest indicated on top are shown in green. Higher magnification of the region between arrowheads is shown on *Top* of each panel (blue, nuclear DAPI; red, cone sheets marked peanut agglutinin lectin [PNA]; magenta, ZO1 marking RPE boundaries for ApoE and C3 panels and Phalloidin marking boundaries for ApoB and CFH panels). (Scale bars: 20 μm.) GCL, ganglion cell layer; RPE, retinal-pigmented epithelium. Images are representatives of three independent experiments on three different animals per genotype. (*K*) Same experiment as in *D* after feeding mice a DHA diet from weaning onwards for 10 wk. Bars show mean ± SEM (*n* = 3 mice, two retinas per mouse; *P < 0.05; **P < 0.01; ****P < 0.0001).

and CFH, and restored C3 expression (Fig. 5*J*). Differences in RPE hypertrophy were not evident, likely because, in younger mice, hypertrophy is not as pronounced yet. None of 12 DHA-fed mice (*n* = 12) developed any GA by 6M while one out of six mice on the control diet did. Interestingly, reprofiling of the retinal lipids after 10 wk of DHA feeding revealed that levels of di-DHA containing PE and PC lipids were not restored. This suggests that DHA must have acted directly on the RPE to improve overall PRE health (Fig. 5*K*). In all, the data indicated that activated mTORC1 in rods affects the retinal lipid composition, which affects overall RPE health.

Cones Contribute Differently than Rods to Disease. Differences in the metabolic needs of rods and cones have been proposed to

contribute to different kinds of deposits (8, 14). To more closely mimic the human retina outside the fovea and study the contribution of cones to advanced pathologies, we generated a line with a cone-specific deletion of *Tsc1* ($^{cone}Tsc1^{-/-}$) and one with a rod-and-cone deletion ($^{cone\&rod}Tsc1^{-/-}$). Funduscopy and angiography revealed that $^{cone}Tsc1^{-/-}$ mice develop similar pathologies without the formation of retinal folds (Fig. 6*A*). Combining the metabolic changes in rods and cones did not increase the overall frequency of advanced pathologies by 12M. However, advanced pathologies started to occur already at 4M (Fig. 6*A*). Choroidal neovascular pathologies in $^{cone}Tsc1^{-/-}$ mice were easier to identify on RPE flat mounts when compared to $^{rod}Tsc1^{-/-}$ mice (Fig. 6*B*). $^{cone}Tsc1^{-/-}$ and $^{cone\&rod}Tsc1^{-/-}$ mice also developed

large drusen-like deposits that were positive for ApoE (Fig. 6 *C* and *D*). Such large deposits were not seen in $^{rod}Tsc1^{-/-}$ mice. EM analyses revealed that loss of *Tsc1* in cones was sufficient to cause accumulation of small lipoprotein vesicles, reminiscent of basal linear deposits, within the BrM (Fig. 6*E*), which may explain the difference in deposit size. Finally, areas of GA were generally larger in $^{cone\&rod}Tsc1^{-/-}$ mice when compared with $^{rod}Tsc1^{-/-}$ or $^{cone}Tsc1^{-/-}$ mice (Fig. 6*F*). This allowed visualization of ongoing RPE atrophy by terminal deoxynucleotidyltransferase-mediated dUTP nick end labeling (TUNEL) (Fig. 5*F*). All other pathologies, such as uniform accumulation of lipoproteins and changes in C3 and CFH expression, were similar between all three lines, with the $^{cone}Tsc1^{-/-}$ mice displaying the least pronounced changes (*SI Appendix*, Fig. S7 *A* and *B*). Rod POS clearance was also affected in $^{cone}Tsc1^{-/-}$ mice, suggesting that our previous findings were not due to an increase in the shedding rate of rod POSs, since loss of *Tsc1* in cones affects rod POS clearance, too. (*SI Appendix*, Fig. S7C). Di-DHA PE lipids were also significantly reduced in $^{cone}Tsc1^{-/-}$ mice (*SI Appendix*, Fig. S7D), suggesting that any reduction in di-DHA PE lipids may affect RPE health. Interestingly, activation of mTORC1 upon loss of *Tsc1* was stronger in cones when compared to rods (*SI Appendix*, Fig. S7E) (26). How this affects cell metabolism remains to be investigated. However, this might in part explain how the relatively low number of cones in mouse might still be able to cause advanced pathologies. In all, the data show that there are distinct mechanisms between rods and cones that contributed to advanced AMD pathologies, which is in line with the findings in humans (8, 14).

Discussion

Age-related macular degeneration is as a multifactorial disease of unclear etiology. Here, we show that altering the metabolic profile of PRs is sufficient to cause 1) changes in ApoB, ApoE, C3, and CFH accumulation at the BrM, 2) formation of drusen-like deposits, and 3) GA and neovascular pathologies. The fact that these mice develop advanced AMD-like pathologies at the same frequency as humans, and that pathologies can be ameliorated by dietary DHA supplementation, suggests that our mouse model may be a valuable tool to study the progression of human AMD. How does our data complement the current understanding of AMD disease progression?

Histopathological analyses indicate that the early disease stages start with the formation of a lipid wall at the choroid–retinal blood barrier, affecting primarily the BrM and the RPE basal lamina (oil spill model) (8, 14). This likely impedes the transfer of hydrophilic molecules such as glucose from the choroidal circulation to PRs. From our studies on retinitis pigmentosa, we know that PRs respond to a reduction in glucose availability by increasing the expression of HK2 and PKM2 through increased mTORC1 activity (18, 21, 22, 43). This helps improve glucose uptake and to redirect a larger percentage of the remaining glucose into the anabolic pathway, which helps maintain POS growth (18, 21, 22, 43). Indeed, we found increased expression of PKM2 and HK2 in PRs of AMD patients. Additionally, PKM2 autoantibodies have been found in AMD patients, independent of the disease stage (30), suggesting that this PR adaptive response is an early reaction of PRs to the formation of the initial lipid wall. By activating mTORC1 in PRs, we thus mimic the adaptive response of PRs to the formation of the initial lipid wall. Since lipid accumulation occurs in all of our models, the metabolic adaptations by PRs further contribute to drusen growth. However, large drusen (>60 µm in diameter) as in humans were not seen in our mice. This is likely because the initial lipid wall, which serves as a foundation for further drusen growth, is not present at the start of our experiments. Additionally, large soft-drusen are preferentially associated with the metabolism of foveal cones (8, 14), which are absent in mouse. Based on our findings, we propose a two-stage process of AMD pathogenesis. In the first stage (*SI Appendix*, Fig. S8), environmental and/or genetic risk factors, such as diet, exercise, and metabolic risk genes, lead to the formation of a lipid wall at the BrM, as proposed by others (8, 44, 45). In the second stage, PR adaptations to the reduction in nutrient transfer further enhance lipid accumulation, while also causing excessive RPE stress. This causes RPE atrophy, GA, and neovascular pathologies, as seen in our mouse models and in humans (15, 39, 40, 46). While this second stage continues to be affected by the same risk factors as the first stage, other risk genes, such as the ones of the innate immune system like C3 and CFH, increase the risk for disease progression (3, 8, 44, 45). The involvement of PRs in disease pathogenesis, which is also supported by a recent RNA sequencing study (47), may also explain why AMD preferentially affects the macular region; it is the area of highest PR density.

The absence of drusen-like deposits in $^{rod}Tsc1^{-/-}$ mice suggests that drusen are not required for RPE atrophy or neovascular pathologies to occur. This suggests that there are PR-intrinsic changes that affect RPE health besides the aggregation of lipoproteins at the BrM. In this regard, we found the drop in di-DHA PE and PC lipid species interesting. DHA-containing phospholipids provide an optimal lipid environment for phototransduction (48) and neuroprotective functions (49, 50). In the retina, these phospholipids account for approximately 15 to 20% PC, 20 to 35% PE, and 30 to 50% PS, with POSs that are phagocytosed daily by the RPE having greater levels (51). The finding that dietary DHA supplementation did not restore retinal di-DHA PE and PC levels suggests that the enzymes required for the synthesis of these lipids were down-regulated as a result of increased mTORC1 activity. mTORC1 is a key regulator of lipid metabolism, in part through regulation of the sterol regulatory element-binding protein 1 and 2 (SREBP-1 and SREBP-2) (25). Further support for altered lipid metabolism comes from a human study that profiled total retinal and RPE/choroid fatty acids. The study found that total retinal and RPE/choroid DHA levels in humans with AMD were reduced by ~29% and ~45%, respectively (52). Together, these findings may explain why, contrary to the prediction of many epidemiological studies (9, 10), the AREDS2 study (53) did not find an association between risk reduction and DHA supplementation. If, in AMD patients, DHA acts directly on the RPE to reduce RPE stress, then the nutritional intake of DHA may need to be high in order to benefit the RPE: in particular, the RPE opposing foveal cones. This is because rods siphon off most of the free DHA that enters the eye (11). Additionally, if the RPE prefers these two specific di-DHA phospholipids as a DHA source for proper cellular function, then exogenous levels that are not PR-derived may need to be higher in order to have a beneficial effect on RPE health. Our study was based on a study that showed a protective effect with five times higher levels of omega-3 fatty acids (42) than the AREDS2 study. It is important to note that we do not think that the reduction in these di-DHA phospholipid species is the sole underlying cause for disease progression; rather, by reducing overall RPE stress, they reduce the risk for progression. The role of these two di-DHA phospholipids in RPE health remains to be investigated. Similarly, how DHA supplementation reduced RPE stress remains to be determined. However, DHA serves as a precursor for the synthesis of RPE-derived neuroprotectin D1, and PE lipids have been found to positively regulate autophagy and reduce age-related oxidative stress and cell death (49–51). Additionally, DHA has been found to have antiinflammatory properties regulating many aspects of the immune system (54). Thus, the protective effect of DHA seen here could be occurring at multiple levels.

The finding that heterozygous *Raptor* mice with intermediate mTORC1 activity did not develop advanced pathologies suggests that these pathologies are driven in a dose-dependent manner by mTORC1. Consistent with this, some of the early pathologies displayed a more intermediate phenotype. Interestingly, in heterozygous *Raptor* mice ($^{rod}Tsc1^{-/-}$ $^{rod}Raptor^{+/-}$), PKM2 levels
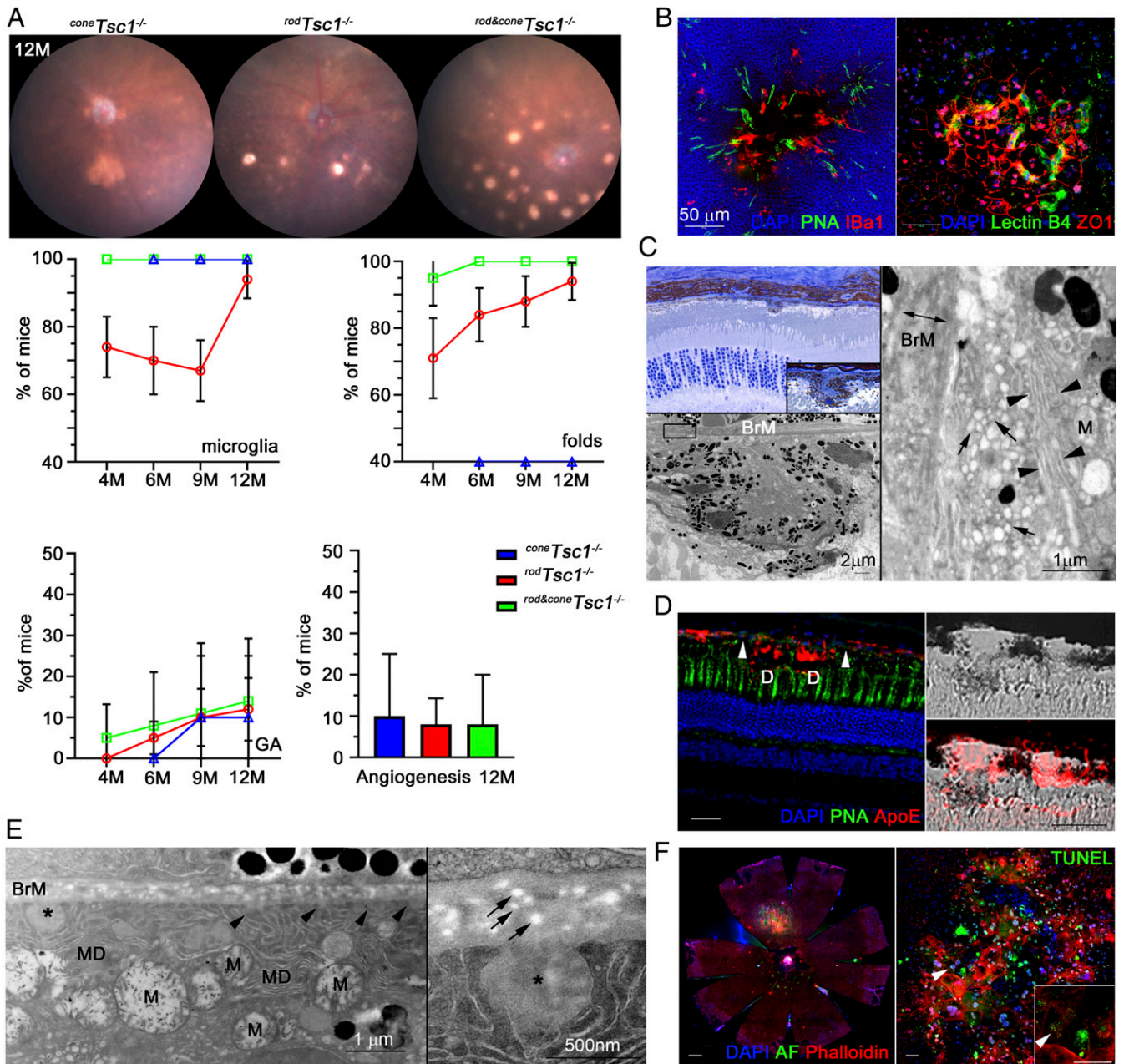
Fig. 6. Cones contribute differently than rods to disease. (*A*) Representative fundus images at 12M (*Top*) and percentage distribution of pathologies (graphs *Below*: microglia accumulation, *Top Left*; retinal folds, *Top Right*; GA, *Bottom Left*; angiogenesis, *Bottom Right*) seen over time of genotypes indicated (M, months). Graphs show percentage ± M.O.E. (n = 10–15 mice). (*B*) $^{cone}Tsc1^{-/-}$ mouse at 12M showing PR atrophy on retinal flat mount with retinal microglia migrating to the site of injury (*Left*) and choroidal neovascularization on corresponding RPE flat mount of the same region (*Right*). Eye corresponds to fundus of $^{cone}Tsc1^{-/-}$ shown in *A*. (Scale bar: 50 μm.) Colors are as indicated by labels in panels (blue, nuclear DAPI; green, cone sheets marked by peanut agglutinin lectin [PNA] or vascular marked with lectin B4 [Lectin B4]; red, microglia marked by Iba1 or RPE boundaries marked by ZO1). (*C*) Semithin section image of $^{cone}Tsc1^{-/-}$ mouse at 12M showing large drusen-like deposit (see *Inset*). (*Below*) EM image of deposit and to the *Right* higher magnification of boxed area in EM image. The BrM is marked by a double arrow. Arrowheads mark RPE basal fold, and arrows mark translucent lipid vesicles. (*D*) Large drusen-like deposits marked with letter D in $^{rod\&cone}Tsc1^{-/-}$ mouse at 12M showing accumulation of ApoE (red signal). Enlarged area between arrowheads of *Left* image is shown to the *Right* in bright field. (Scale bars: 20 μm.) Colors are as indicated by labels in panel (blue, nuclear DAPI; green, cone sheets marked by peanut agglutinin lectin [PNA]; red, deposits positive for ApoE). (*E*) EM images of $^{cone}Tsc1^{-/-}$ mouse at 12M showing basal mounds (asterisk, larger mound; arrowheads, micro mounds), lipoprotein vesicles in the BrM (arrows), dysmorphic mitochondria (M), and membranous discs (MD). (*Right*) Enlarged area of basal mound marked with asterisk on the left showing lipoprotein vesicles in BrM (arrows). (*F*) Large GA area in $^{rod\&cone}Tsc1^{-/-}$ mouse at 12M showing TUNEL-positive RPE cells. *Left* panel shows RPE whole mount, while *Right* panel shows higher magnification of GA area surrounded by dysmorphic RPE cells and TUNEL-positive nuclei (arrowheads). *Inset* shows higher magnification of TUNEL-positive nuclei. (Scale bars: *Left*, 300 μm; *Right*, 15 μm.) Colors are as indicated by labels in panels (blue, nuclear DAPI; green, autofluorescence [AF] in *Left* panel and apoptosis marked by TUNEL in *Right* panel; red, RPE boundaries marked by Phalloidin).

remained high while lactate and NADPH levels dropped to Cre^- control levels. Therefore, it remains to be investigated to which extent changes in the energy ecosystem between PRs and RPE

contribute to advanced pathologies (15, 20, 55, 56). However, it is important to note that the circumstances in which PRs find themselves in AMD retinas and in our mouse model differ since

Cheng et al.

glucose is not limiting in our experiments due to the absence of a lipid wall. Nonetheless, our mice develop the same intermediate and advanced pathologies as seen in humans with AMD. This suggests that changes in the exchange of glucose and lactate between the retina and RPE are less likely to be the driving force for the development of advanced pathologies as these differ between our mouse models and AMD patients. Rather, the data suggest that gene expression changes that accompany the adaptations to a glucose shortage cause disease progression (e.g., down-regulation of enzymes that cause drop in di-DHA phospholipids). In line with this, DHA feeding was able to ameliorate most pathologies. While we did not measure lactate and NADPH levels in DHA-fed $^{rod}TSC1^{-/-}$ mice, one would not expect that this feeding regimen would restore lactate and NADPH levels to Cre^- control levels. The disruption in the energy ecosystem between the PRs and the RPE in $^{rod}TSC1^{-/-}$ mice is thus unlikely to be the driving force for the pathologies seen in these mice. It remains to be investigated which changes downstream of mTORC1 lead to disease progression in our mouse models. Identifying these changes is important since these changes may not require high mTORC1 activity in humans to cause disease. Once identified, they would allow us to study how much our mouse model parallels the human disease. Moreover, it might also offer new therapeutic targets to delay disease progression in humans if such changes are confirmed in humans. There are likely several changes that are required to occur, either simultaneously or sequentially, in order for advanced pathologies to develop. This means that preventing one of the changes to occur might suffice to delay disease progression. Because advanced pathologies are dependent on the dose of activated mTORC1 in mouse, one might also considering decreasing mTORC1 activity. In this regard, mTORC1 inhibitors have already been used in several clinical trials on patients with advanced AMD (57, 58). However, these trials reported either no effect or even some adverse effects resulting in reduced vision. The likely explanation for this is that inhibiting mTORC1 activity in patients with advanced disease affects PR survival as mTORC1 activity is required to help PRs adapt to the nutrient stress that they are experiencing due to lost or dysfunctional RPE cells. We previously reported that mTORC1 activity is required for the survival of metabolically stressed PRs (18, 22, 43), in particular in areas of

GA (26). Reducing mTORC1 activity during the early disease stages might be more beneficial. In line with this, a retrospective study found that the antidiabetic drug Metformin, which reduces mTORC1 activity by activating AMP kinase, reduces the risk for developing AMD (59). More studies are needed to determine the correct time window and dose of mTORC1 inhibition in humans. Additionally, identifying the downstream factors that lead to advanced disease may allow one to block disease progression without preventing PRs from adapting to the nutrient shortage. In all, our findings complement the current model of AMD pathogenesis, showing in mouse that activation of mTORC1 in PRs leads to the development of a complex pathology that affects overall RPE health over time.

Materials and Methods

All procedures involving animals were in compliance with the Association for Research in Vision and Ophthalmology Statement for the Use of Animals in Ophthalmic and Vision Research and were approved by the Institutional Animal Care and Use Committees of the University of Massachusetts Medical School. Procurement of human samples by B.P.H. was approved by the Partners Institutional Review Board. The Institutional Review Board of the University of Massachusetts issued a waiver to C.P. to work with deidentified human tissue sections since he was not involved in procuring human tissue. Similarly, the Institutional Review Board of the University of Connecticut issued a waiver to R.N.K. to work with deidentified tissue samples. Tissue sample contributed by R.N.K. was procured under an approved protocol by Institutional Review Board of the University of Connecticut through the University of Connecticut Health Center. R.N.K. received only deidentified tissue that was contributed to this study. Extensive materials and methods regarding all procedures are provided in *SI Appendix, Materials and Methods*.

Data Availability. All data and experimental parameters related to this paper are available in the main text and *SI Appendix*.

1. J. W. Miller, Age-related macular degeneration revisited–piecing the puzzle: The LXIX Edward Jackson memorial lecture. *Am. J. Ophthalmol.* **155**, 1–35.e13 (2013).
2. K. L. Pennington, M. M. DeAngelis, Epidemiology of age-related macular degeneration (AMD): Associations with cardiovascular disease phenotypes and lipid factors. *Eye Vis. (Lond.)* **3**, 34 (2016).
3. M. J. Geerlings, E. K. de Jong, A. I. den Hollander, The complement system in age-related macular degeneration: A review of rare genetic variants and implications for personalized treatment. *Mol. Immunol.* **84**, 65–76 (2017).
4. M. P. Kawa, A. Machalinska, D. Roginska, B. Machalinski, Complement system in pathogenesis of AMD: Dual player in degeneration and protection of retinal tissue. *J. Immunol. Res.* **2014**, 483960 (2014).
5. R. Reynolds, B. Rosner, J. M. Seddon, Dietary omega-3 fatty acids, other fat intake, genetic susceptibility, and progression to incident geographic atrophy. *Ophthalmology* **120**, 1020–1028 (2013).
6. J. P. SanGiovanni *et al.*; Age-Related Eye Disease Study Research Group, The relationship of dietary lipid intake and age-related macular degeneration in a case-control study: AREDS Report No. 20. *Arch. Ophthalmol.* **125**, 671–679 (2007).
7. L. Wang *et al.*, Abundant lipid and protein components of drusen. *PLoS One* **5**, e10329 (2010).
8. C. A. Curcio, Soft drusen in age-related macular degeneration: Biology and targeting via the oil spill strategies. *Invest. Ophthalmol. Vis. Sci.* **59**, AMD160-AMD181 (2018).
9. E. H. Souied *et al.*, Omega-3 fatty acids and age-related macular degeneration. *Ophthalmic Res.* **55**, 62–69 (2015).
10. B. M. Merle *et al.*, High concentrations of plasma n3 fatty acids are associated with decreased risk for late age-related macular degeneration. *J. Nutr.* **143**, 505–511 (2013).
11. M. P. Agbaga *et al.*, Differential composition of DHA and very-long-chain PUFAs in rod and cone photoreceptors. *J. Lipid Res.* **59**, 1586–1596 (2018).
12. R. N. Khurana *et al.*, Rapid recurrence of geographic atrophy after full macular translocation for nonexudative age-related macular degeneration. *Ophthalmology* **112**, 1586–1591 (2005).
13. M. T. Cahill, P. Mruthyunjaya, C. Bowes Rickman, C. A. Toth, Recurrence of retinal pigment epithelial changes after macular translocation with 360 degrees peripheral retinectomy for geographic atrophy. *Arch. Ophthalmol.* **123**, 935–938 (2005).
14. C. A. Curcio, Antecedents of soft drusen, the specific deposits of age-related macular degeneration, in the biology of human Macula. *Invest. Ophthalmol. Vis. Sci.* **59**, AMD182-AMD194 (2018).
15. C. R. Fisher, D. A. Ferrington, Perspective on AMD pathobiology: A bioenergetic crisis in the RPE. *Invest. Ophthalmol. Vis. Sci.* **59**, AMD41-AMD47 (2018).
16. A. Rajala *et al.*, Pyruvate kinase M2 regulates photoreceptor structure, function, and viability. *Cell Death Dis.* **9**, 240 (2018).
17. A. Rajala, Y. Wang, K. Soni, R. V. S. Rajala, Pyruvate kinase M2 isoform deletion in cone photoreceptors results in age-related cone degeneration. *Cell Death Dis.* **9**, 737 (2018).
18. L. Petit *et al.*, Aerobic glycolysis is essential for normal rod function and controls secondary cone death in retinitis pigmentosa. *Cell Rep.* **23**, 2629–2642 (2018).
19. Y. Chinchore, T. Begaj, D. Wu, E. Drokhlyansky, C. L. Cepko, Glycolytic reliance promotes anabolism in photoreceptors. *eLife* **6**, e25946 (2017).
20. M. A. Kanow *et al.*, Biochemical adaptations of the retina and retinal pigment epithelium support a metabolic ecosystem in the vertebrate eye. *eLife* **6**, e28899 (2017).
21. C. Punzo, K. Kornacker, C. L. Cepko, Stimulation of the insulin/mTOR pathway delays cone death in a mouse model of retinitis pigmentosa. *Nat. Neurosci.* **12**, 44–52 (2009).
22. A. Venkatesh *et al.*, Activated mTORC1 promotes long-term cone survival in retinitis pigmentosa mice. *J. Clin. Invest.* **125**, 1446–1458 (2015).
23. Q. Sun *et al.*, Mammalian target of rapamycin up-regulation of pyruvate kinase isoenzyme type M2 is critical for aerobic glycolysis and tumor growth. *Proc. Natl. Acad. Sci. U.S.A.* **108**, 4129–4134 (2011).
24. R. Zoncu, A. Efeyan, D. M. Sabatini, mTOR: from growth signal integration to cancer, diabetes and ageing. *Nat. Rev. Mol. Cell Biol.* **12**, 21–35 (2011).
25. K. Düvel *et al.*, Activation of a metabolic gene regulatory network downstream of mTOR complex 1. *Mol. Cell* **39**, 171–183 (2010).
26. M. Zieger, C. Punzo, Improved cell metabolism prolongs photoreceptor survival upon retinal-pigmented epithelium loss in the sodium iodate induced model of geographic atrophy. *Oncotarget* **7**, 9620–9633 (2016).
27. A. Polchi, A. Magini, D. D. Meo, B. Tancini, C. Emiliani, mTOR signaling and neural stem cells: The tuberous sclerosis complex model. *Int. J. Mol. Sci.* **19**, E1474 (2018).

NEUROSCIENCE

28. K. C. Patra *et al.*, Hexokinase 2 is required for tumor initiation and maintenance and its systemic deletion is therapeutic in mouse models of cancer. *Cancer Cell* **24**, 213–228 (2013).

29. T. L. Dayton, T. Jacks, M. G. Vander Heiden, PKM2, cancer metabolism, and the road ahead. *EMBO Rep.* **17**, 1721–1730 (2016).

30. K. Morohoshi *et al.*, Identification of anti-retinal antibodies in patients with age-related macular degeneration. *Exp. Mol. Pathol.* **93**, 193–199 (2012).

31. H. Gu, J. D. Marth, P. C. Orban, H. Mossmann, K. Rajewsky, Deletion of a DNA polymerase beta gene segment in T cells using cell type-specific gene targeting. *Science* **265**, 103–106 (1994).

32. W. Ma, W. T. Wong, Aging changes in retinal microglia and their relevance to age-related retinal disease. *Adv. Exp. Med. Biol.* **854**, 73–78 (2016).

33. J. Z. Chuang, S. Y. Chou, C. H. Sung, Chloride intracellular channel 4 is critical for the epithelial morphogenesis of RPE cells and retinal attachment. *Mol. Biol. Cell* **21**, 3017–3028 (2010).

34. R. Longbottom *et al.*, Genetic ablation of retinal pigment epithelial cells reveals the adaptive response of the epithelium and impact on photoreceptors. *Proc. Natl. Acad. Sci. U.S.A.* **106**, 18728–18733 (2009).

35. Y. Chen, J. Wang, J. Cai, P. Sternberg, Altered mTOR signaling in senescent retinal pigment epithelium. *Invest. Ophthalmol. Vis. Sci.* **51**, 5314–5319 (2010).

36. B. Yu *et al.*, Subcellular distribution and activity of mechanistic target of rapamycin in aged retinal pigment epithelium. *Invest. Ophthalmol. Vis. Sci.* **55**, 8638–8650 (2014).

37. J. Huang *et al.*, Abnormal mTORC1 signaling leads to retinal pigment epithelium degeneration. *Theranostics* **9**, 1170–1180 (2019).

38. M. R. Kozlowski, RPE cell senescence: A key contributor to age-related macular degeneration. *Med. Hypotheses* **78**, 505–510 (2012).

39. N. Golestaneh, Y. Chu, Y. Y. Xiao, G. L. Stoleru, A. C. Theos, Dysfunctional autophagy in RPE, a contributing factor in age-related macular degeneration. *Cell Death Dis.* **8**, e2537 (2017).

40. K. Kaarniranta *et al.*, Autophagy and heterophagy dysregulation leads to retinal pigment epithelium dysfunction and development of age-related macular degeneration. *Autophagy* **9**, 973–984 (2013).

41. B. L. Scott, E. Racz, R. N. Lolley, N. G. Bazan, Developing rod photoreceptors from normal and mutant rd mouse retinas: Altered fatty acid composition early in development of the mutant. *J. Neurosci. Res.* **20**, 202–211 (1988).

42. T. Georgiou, E. Prokopiou, The new era of omega-3 fatty acids supplementation: Therapeutic effects on dry age-related macular degeneration. *J. Stem Cells* **10**, 205–215 (2015).

43. A. Venkatesh, S. Ma, C. Punzo, TSC but not PTEN loss in starving cones of retinitis pigmentosa mice leads to an autophagy defect and mTORC1 dissociation from the lysosome. *Cell Death Dis.* **7**, e2279 (2016).

44. L. G. Fritsche *et al.*, Age-related macular degeneration: Genetics and biology coming together. *Annu. Rev. Genomics Hum. Genet.* **15**, 151–171 (2014).

45. L. G. Fritsche *et al.*, A large genome-wide association study of age-related macular degeneration highlights contributions of rare and common variants. *Nat. Genet.* **48**, 134–143 (2016).

46. E. Keeling, A. J. Lotery, D. A. Tumbarello, J. A. Ratnayaka, Impaired cargo clearance in the retinal pigment epithelium (RPE) underlies irreversible blinding diseases. *Cells* **7**, E16 (2018).

47. M. Menon *et al.*, Single-cell transcriptomic atlas of the human retina identifies cell types associated with age-related macular degeneration. *Nat. Commun.* **10**, 4902 (2019).

48. M. Neuringer, W. E. Connor, D. S. Lin, L. Barstad, S. Luck, Biochemical and functional effects of prenatal and postnatal omega 3 fatty acid deficiency on retina and brain in rhesus monkeys. *Proc. Natl. Acad. Sci. U.S.A.* **83**, 4021–4025 (1986).

49. N. G. Bazan, Docosanoids and elovanoids from omega-3 fatty acids are pro-homeostatic modulators of inflammatory responses, cell damage and neuroprotection. *Mol. Aspects Med.* **64**, 18–33 (2018).

50. P. Rockenfeller *et al.*, Phosphatidylethanolamine positively regulates autophagy and longevity. *Cell Death Differ.* **22**, 499–508 (2015).

51. F. Li, H. Chen, R. E. Anderson, Biosynthesis of docosahexaenoate-containing glycerolipid molecular species in the retina. *J. Mol. Neurosci.* **16**, 205–214, NaN–221 (2001).

52. A. Liu, J. Chang, Y. Lin, Z. Shen, P. S. Bernstein, Long-chain and very long-chain polyunsaturated fatty acids in ocular aging and age-related macular degeneration. *J. Lipid Res.* **51**, 3217–3229 (2010).

53. Age-Related Eye Disease Study 2 Research Group, Lutein + zeaxanthin and omega-3 fatty acids for age-related macular degeneration: The age-related eye disease study 2 (AREDS2) randomized clinical trial. *JAMA* **309**, 2005–2015 (2013).

54. S. Gutiérrez, S. L. Svahn, M. E. Johansson, Effects of omega-3 fatty acids on immune cells. *Int. J. Mol. Sci.* **20**, E5028 (2019).

55. D. A. Ferrington *et al.*, Altered bioenergetics and enhanced resistance to oxidative stress in human retinal pigment epithelial cells from donors with age-related macular degeneration. *Redox Biol.* **13**, 255–265 (2017).

56. L. Xu, L. Kong, J. Wang, J. D. Ash, Stimulation of AMPK prevents degeneration of photoreceptors and the retinal pigment epithelium. *Proc. Natl. Acad. Sci. U.S.A.* **115**, 10475–10480 (2018).

57. P. A. Petrou *et al.*, Intravitreal sirolimus for the treatment of geographic atrophy: Results of a phase I/II clinical trial. *Invest. Ophthalmol. Vis. Sci.* **56**, 330–338 (2014).

58. W. T. Wong *et al.*, Treatment of geographic atrophy with subconjunctival sirolimus: Results of a phase I/II clinical trial. *Invest. Ophthalmol. Vis. Sci.* **54**, 2941–2950 (2013).

59. E. E. Brown *et al.*, The common antidiabetic drug Metformin reduces odds of developing age-related macular degeneration. *Invest. Ophthalmol. Vis. Sci.* **60**, 1470–1477 (2019).

Cheng et al.

Supporting Information Appendix

Material & Methods:

Human tissue samples. Age and sex of human postmortem eye samples are indicated in figures. Procurement of human samples by B.H was approved by the Partners Institutional Review Board. The Institutional Review Board of the University of Massachusetts issued a waiver to C.P. to work with de-identified human tissue sections since he was not involved in procuring human tissue. Similarly, the Institutional Review Board of the University of Connecticut issued a waiver to R.K. to work with de-identified tissue samples. Tissue sample contributed by R.K. was procured under an approved protocol by Institutional Review Board of the University of Connecticut through the University of Connecticut Health Center. R.K. received only de-identified tissue that was contributed to this study. All staining on human tissue sample used cryo-preserved tissue sections.

Animals. The conditional *Tsc1* (1) and *Raptor* (2) alleles as well as the rod *iCre-75* (3) and cone-Cre (4) have all been previously described. All mice were genotyped for the absence of the *rd8* mutation (5). Mice were kept on a 12hr-light/12hr-dark cycle with unrestricted diets. Equal numbers of male and female mice were used in all experiments. No sex-specific differences were noted. The DHA diet was made by replacing 2% of soybean oil in the AIN-93G lab diet from Dyets, Inc., (https://dyets.com) with 2% DHASCO from DSM (https://www.dsm.com/corporate/home.html). The AIN-93G diet was used as a control diet for all DHA experiments. Except for the DHA and DHA control experiments, all animals were kept on the diet provided by the mouse facility of the University (5P75* from https://www.labdiet.com/). The AIN-93G control diet and the 5P75* facility diet differ in their soybean oil content, which are 7% and 5%, respectively. All procedures involving animals were in compliance with the Association for Research in Vision and Ophthalmology (ARVO) Statement for the Use of Animals in Ophthalmic and Vision Research and were approved by the Institutional Animal Care and Use Committees (IACUC) of the University of Massachusetts Medical School.

Funduscopy and angiography. Funduscopy was performed as previously described (6). Ages and number of mice analyzed for a given experiment are indicated in figures and/or legends. Angiography was performed immediately following funduscopy imaging by injecting 125 mg/kg of a fluorescein sodium solution subcutaneously behind the neck. Images were acquired with the Micron III from Phoenix Technology Group. Overall accuracy of GA diagnosis by funduscopy was confirmed on RPE flat mounts of 22 eyes, 7 of which were diagnosed with GA by funduscopy. Of the 22 eyes, 9 were confirmed on RPE flat mounts to have GA, indicating that the percentage reported in the study may be slightly lower than the actual percentage.

Optical coherence tomography (OCT). OCT was performed with a system from Bioptigen (Model: 70-20000). OCT in Figure S3 was acquired during manuscript revision with a new Micron IV system from Phoenix Technology Group. Mice were anesthetized with a mixture of ketamine/xylazine (100 mg/kg and 10 mg/kg). One drop of both Phenylephrine (2.5%) and Tropicamide (1%) was applied for pupil dilation 10 min prior to recording. After the recording mice were allowed to recover on a warm heating tray.

Electroretinography (ERG) analysis. ERGs were performed with the Celeris system (Diagnosys LLC) and their preset programs for scotopic, photopic and C-wave ERGs. Handling of the animals was performed as previously described (7). Number of mice per group is indicated in figure legend. Mice were not pre-screened for their eye pathologies.

Lactate assay. Lactate assay (L-Lactate Assay kit, Abcam, Cat# ab65330) was performed with 2-month-old mice using 4 biological samples, each composed of both retinas from the same animal. Each biological measurement was performed in triplicate. Retinas were dissected in ice cold PBS and processed according to manufacturer's instructions.

NADPH assay. NADPH assay (NADP/NADPH Assay Kit, Sigma, Cat# MAK312) was performed with 2-month-old mice using 7-8 biological samples, each composed of one retina. Each biological measurement was performed in duplicate. Retinas were dissected in ice cold PBS and processed according to manufacturer's instructions.

Quantitative Western blot analyses. All Western blot quantifications used 3 biological samples with each sample consisting of both retinas from the same mouse. The analysis of each sample was performed in triplicate. Proteins were extracted as follows: enucleated eyes were dissected in cold PBS buffer. Dissected retinas were immediately transferred into RIPA buffer (Thermo Scientific, cat# 89900) with protease & phosphatase inhibitors (1:100 dilution; cat#1861281) and homogenized by sonication. After 10 min centrifugation at 4°C at 13000 RPM, protein extracts were transferred into a fresh tube and protein concentration was quantified with the Bio-Rad Protein Assay (cat# 500-0113,0114,0115). To quantify PKM2 and p-S6 expression levels, 5μg and 10μg of total protein, respectively, were loaded. The following primary antibodies from Cell Signaling Technology were used: rabbit anti-PKM2 antibody (1:4,000; Cat#4053), rabbit anti-pS6 (Ser240/244) (1:1000; Cat#5364), and for normalization mouse anti-β-actin antibody (1:1,000, Cat#3700). Protein detection was done using fluorescently labeled secondary (1:10,000) antibodies from Licor in combination with the Odyssey system. Quantification was performed with Image Studio software. The combination of these tools allows for optimal linear quantification independent of any post-acquisition image modifications for visualization purposes.

Immunohistochemistry. Immunohistochemistry (IHC) and immunofluorescence on either cryo-preserved sections (10μm thickness) or RPE/retina whole mounts were performed as described previously (6, 8-10). The following primary antibodies were used: rabbit anti-PKM2 (1:1000; Cell Signaling Technology, Cat#4053), rabbit anti-ZO1 (1:100; Invitrogen, Cat#40-2200), and rabbit anti-Iba1 (1:300; Wako, Cat#019-19741), mouse anti-CRE-Recombinase (1:500, Covance, Cat#PRB-106P), mouse anti-Rhodopsin (1:100, originally obtained from the University of British Columbia, Clone 1D4, available from Abcam, cat# 5417) all diluted in PBS with 0.3% Triton X-100 and 5% bovine serum albumin (BSA, Cell Signaling Technology). For the rabbit anti-pS6 (Ser240/244) antibody (1:300; Cell Signaling Technology, Cat# 5364), PBS was replaced with TBS. For the rabbit anti-Apolipoprotein B (ApoB) (1:800; Abcam, Cat# 20737), goat anti-Apolipoprotein E (ApoE) (1:1,000, Millipore, Cat#178479), rabbit anti-CFH (1:300; Cat# ABIN3023097) and goat

anti-mouse complement C3 (1:300; MP Biomedicals, cat# 55510), Triton X-100 was replaced with 0.2% Saponin. The following reagents already had a chromophore conjugated: rhodamine phalloidin (1:1,000; Life Technologies, Cat# R415), fluorescein peanut agglutinin lectin (PNA) (1:1,000; Vector Laboratories, Cat# FL1071) and fluorescein Griffonia Simplicifonia Lectin I (GSL I) isolectin B4 (1:300; Vector Laboratories, Cat# FL-1201). Nuclei were counterstained with 4´, 6-diamidino-2-phenylindole (DAPI) (Sigma-Aldrich, Cat# 9542). All secondary antibodies (1:500, donkey) were purchased from Jackson Immuno Research and were purified F(ab)2 fragments that displayed minimal cross-reactivity with other species. An exception of this was the immunohistochemistry staining in Figure 1A, which used the ImmPACT VIP kit (Vector Laboratories, Cat# SK-4605). Expression changes for ApoB, ApoE, C3 and CFH were confirmed in at least 3 individual animal per genotype. All images were visualized with a Leica DM6 Thunder microscope with a 16 bit monochrome camera.

RPE polynucleation and cell size quantification. RPE whole mounts were collected and stained with anti-ZO1 antibody by immunofluorescence in order to highlight RPE cell boundaries. For quantification, 10 images of 22,500 μm^2 each were selected within a radius of 1.5 mm from the center. Because the distribution of affected regions can be random in control and experimental mice, the 10 most affected areas within one RPE flat mount were selected, avoiding regions of GA in experimental mice. Images for quantification were acquired at 20X. IMARIS software was used to quantify the number of nuclei and cell area of each RPE cell within a given image. Each image had 30-50 RPE cells, meaning per RPE flat mount we analyzed 300-500 RPE cells to calculate the average number of nuclei per RPE cell and the average RPE cell size. Each experimental group consisted of 6-8 RPE flat mounts. The age and number of RPE flat mounts per group is indicated in the corresponding figure legend.

Analysis of POS clearance by the RPE. Quantification of POS clearance was performed similar to other published literature (11) with the following modifications: Per RPE flat mount, 10 areas of 40,000 μm^2 within a 1.5 mm radius from the center were selected randomly to quantify the number

of RHODOPSIN positive dots per RPE cell. Images for quantification were acquired at 20X. RPE cell boundaries were detected with anti-ZO1 antibody. Quantification was performed using IMARIS imaging processor by selecting a dot diameter >2 μm to count dots and by counting the number of RPE cells per imaged field. The average dot number per RPE cell for a given RPE flat mount was obtained by averaging the results of the 10 fields. This number was then used to generate the average of the biological replicates, as indicated in the individual figures, per genotype and time point. All POS clearance experiments were performed with 2M-old mice except for 6M-old mice that were fed the DHA-enriched diet for 2 weeks.

Quantification of rod survival. Quantification of rod survival was performed as previously described (12). Each group used 6 retinas per quantification. Retinal sections were cut in a dorsal to ventral direction.

TUNEL assay. TUNEL assay (Roche, Cat# 12156792910) was performed according to manufacturer's instructions. After the TUNEL reaction, tissue was processed for immunofluorescence staining as described above.

Semithin and transmission electron microscopy (EM) were performed as previously described (7).

Lipid profiling. Each biological sample consists of two retinas from the same animal. The following numbers of biological samples were used: $^{rod}Tsc1^{-/-} = 9$; $^{rod}Tsc1^{+/+} = 6$; $^{cone}Tsc1^{-/-} = 6$; $^{cone\&rod}Tsc1^{-/-} = 3$, and the DHA experiments used 3 biological samples per condition. The POS preparations pooled 6 retinas from 3 animals per genotype. The analytical methods have been described previously (13). Briefly, tissue was homogenized in 40% aqueous methanol and then diluted to a concentration of 1:40 with 2-propanol/methanol/chloroform (4:2:1 v/v/vol) containing 20 mM ammonium formate and 1.0 μM PC (14:0/14:0), 1.0 μM PE (14:0/14:0), and 0.33 μM PS (14:0/14:0) as internal standards. Samples were introduced into a triple-quadrupole mass spectrometer (TSQ Ultra, Thermo Scientific) by using a chip-based nano-ESI source (Advion NanoMate) operating in infusion mode. PC lipids were measured using precursor ion scanning of *m/z* 184, PE lipids were

measured using neutral loss scanning of *m/z* 141, and PS lipids were measured using neutral loss scanning of *m/z* 185. All species detected for each group are represented as a relative percentage of the sum based on their response values. Abundances of lipid molecular species were calculated using the Lipid Mass Spectrum Analysis (LIMSA) software (University of Helsinki, Helsinki, Finland).

Statistical analysis. Multiple t-test was used for two-group comparisons and two-way ANOVA for comparisons of more than two groups. Both analysis types were two-tailed. Significance levels: $*p < 0.05$; $**p < 0.01$; $***p < 0.001$; $****p < 0.0001$. All bar graphs indicate mean and error bars represent the S.E.M. Fundus analysis bar graphs show the percentage of mice that developed the retinal pathologies described while error bars represent margin of errors calculated with 90% confidence.

References:

1. Kwiatkowski DJ*, et al.* (2002) A mouse model of TSC1 reveals sex-dependent lethality from liver hemangiomas, and up-regulation of p70S6 kinase activity in Tsc1 null cells. *Hum Mol Genet* 11(5):525-534.

2. Bentzinger CF*, et al.* (2008) Skeletal muscle-specific ablation of raptor, but not of rictor, causes metabolic changes and results in muscle dystrophy. *Cell Metab* 8(5):411-424.

3. Li S*, et al.* (2005) Rhodopsin-iCre transgenic mouse line for Cre-mediated rod-specific gene targeting. *Genesis* 41(2):73-80.

4. Le YZ*, et al.* (2004) Targeted expression of Cre recombinase to cone photoreceptors in transgenic mice. *Mol Vis* 10:1011-1018.

5. Mattapallil MJ*, et al.* (2012) The Rd8 mutation of the Crb1 gene is present in vendor lines of C57BL/6N mice and embryonic stem cells, and confounds ocular induced mutant phenotypes. *Invest Ophthalmol Vis Sci* 53(6):2921-2927.

6. Venkatesh A, Ma S, Langellotto F, Gao G, & Punzo C (2013) Retinal gene delivery by rAAV and DNA electroporation. *Curr Protoc Microbiol* Chapter 14:Unit 14D 14.

7. Ma S*, et al.* (2015) Loss of mTOR signaling affects cone function, cone structure and expression of cone specific proteins without affecting cone survival. *Exp Eye Res* 135:1-13.

8. Venkatesh A*, et al.* (2015) Activated mTORC1 promotes long-term cone survival in retinitis pigmentosa mice. *J Clin Invest* 125(4):1446-1458.

9. Venkatesh A, Ma S, & Punzo C (2016) TSC but not PTEN loss in starving cones of retinitis pigmentosa mice leads to an autophagy defect and mTORC1 dissociation from the lysosome. *Cell Death Dis* 7(6):e2279.

10. Zieger M & Punzo C (2016) Improved cell metabolism prolongs photoreceptor survival upon retinal-pigmented epithelium loss in the sodium iodate induced model of geographic atrophy. *Oncotarget* 7(9):9620-9633.

11. Law AL*, et al.* (2009) Annexin A2 regulates phagocytosis of photoreceptor outer segments in the mouse retina. *Mol Biol Cell* 20(17):3896-3904.

12. Petit L*, et al.* (2018) Aerobic Glycolysis Is Essential for Normal Rod Function and Controls Secondary Cone Death in Retinitis Pigmentosa. *Cell Rep* 23(9):2629-2642.

13. Busik JV, Reid GE, & Lydic TA (2009) Global analysis of retina lipids by complementary precursor ion and neutral loss mode tandem mass spectrometry. *Methods Mol Biol* 579:33-70.
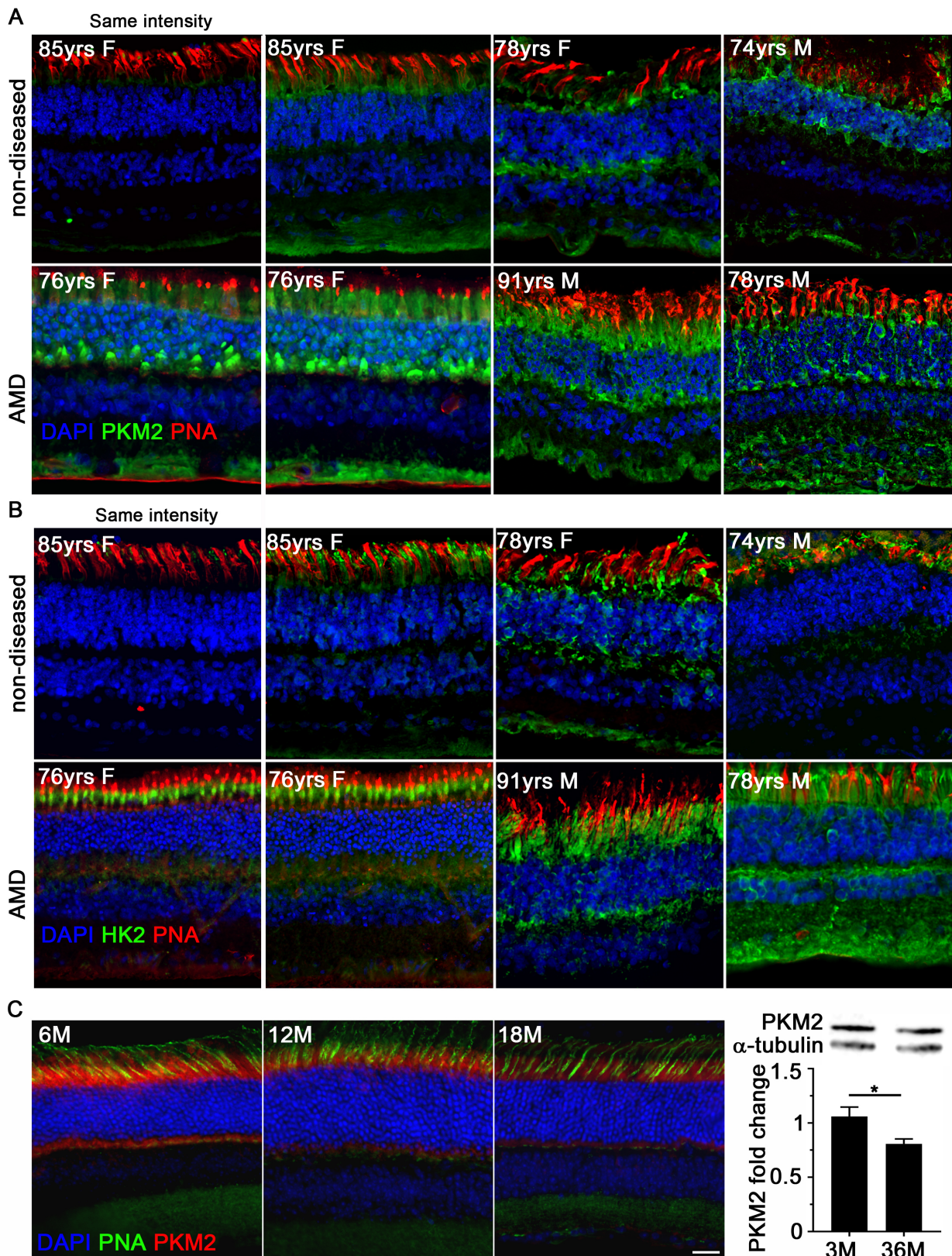
Figure S1. Both PKM2 and HK2 expression are increased in PRs of AMD patients. (A and B) Immunofluorescence for PKM2 (A) and HK2 (B) expressions (green signal) in PRs of non-diseased human donor eyes (top rows) and AMD donor eyes (bottom rows). First two columns are donor retinas shown in Figure 1. First column shows images at same signal intensity between non-disease

8

and diseased tissue. Images in column 2-4 show scaled signal where PKM2 levels have been increased by a factor 2 in non-diseased tissue to better visualize the signal in PRs, while HK2 levels were scaled by a factor of 1.5 in non-diseased tissue. In both cases the baseline signal has also been slightly increased when compared to the panels that show the same intensity (compare diseased tissue from column 1 with 2). Signal is generally stronger in cone pedicels, cone inner segments or throughout the outer nuclear layer in eyes from AMD patients when compared to non-diseased controls. Panel in (A) and (B) within the same column are corresponding sections from the same donor retina. (Blue: nuclear DAPI; red: peanut agglutinin lectin to visualize cone segments; green: PKM2 or HK2 as indicated; F: female; M: male; yrs: years; ages of individuals are indicated in panels in years). (C) Immunofluorescence with the same PKM2 antibody at different ages in mouse showing a decrease of the PKM2 signal with age. Far right: Western blot and quantification for PKM2 with retinas from 3M and 36M old mice showing that total levels decline with age. (n=6 retinas) (*p < 0.05).
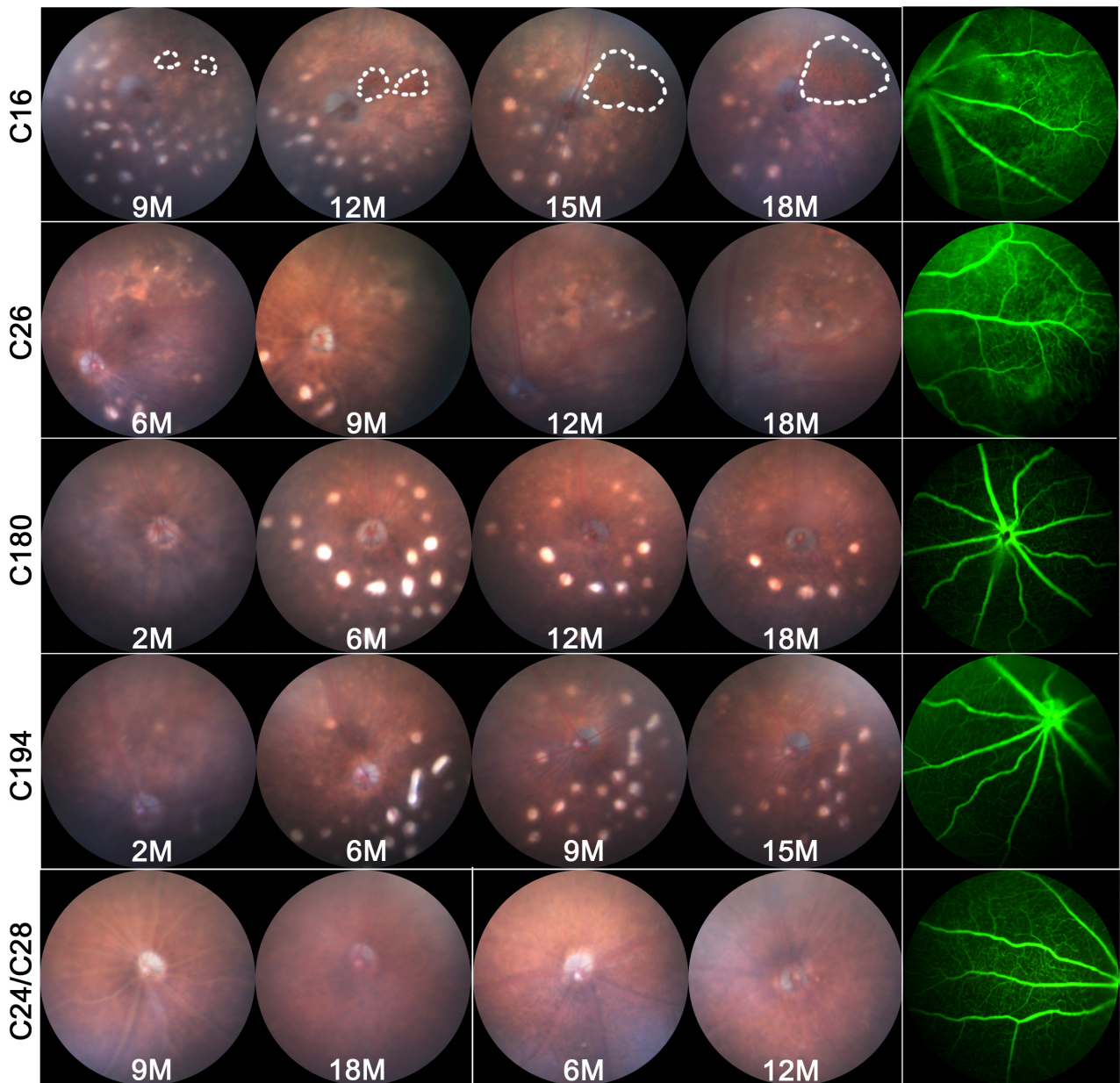
Figure S2. Representative fundus images of the same eye over time. $^{rod}Tsc1^{-/-}$ mice were imaged at indicated ages to trace disease progression within the same animal over time. C16 and C26 mice developed GA (dotted lines) and neovascular pathologies. C180 and C194 developed retinal folds and had microglia migrating into the subretinal space but did not develop advanced pathologies. $^{rod}Tsc1^{+/+}$ mice, C24 and C28, show normal fundus over time. Fundus fluorescein angiography images (right column) shown are of fundus image of the oldest age indicated.
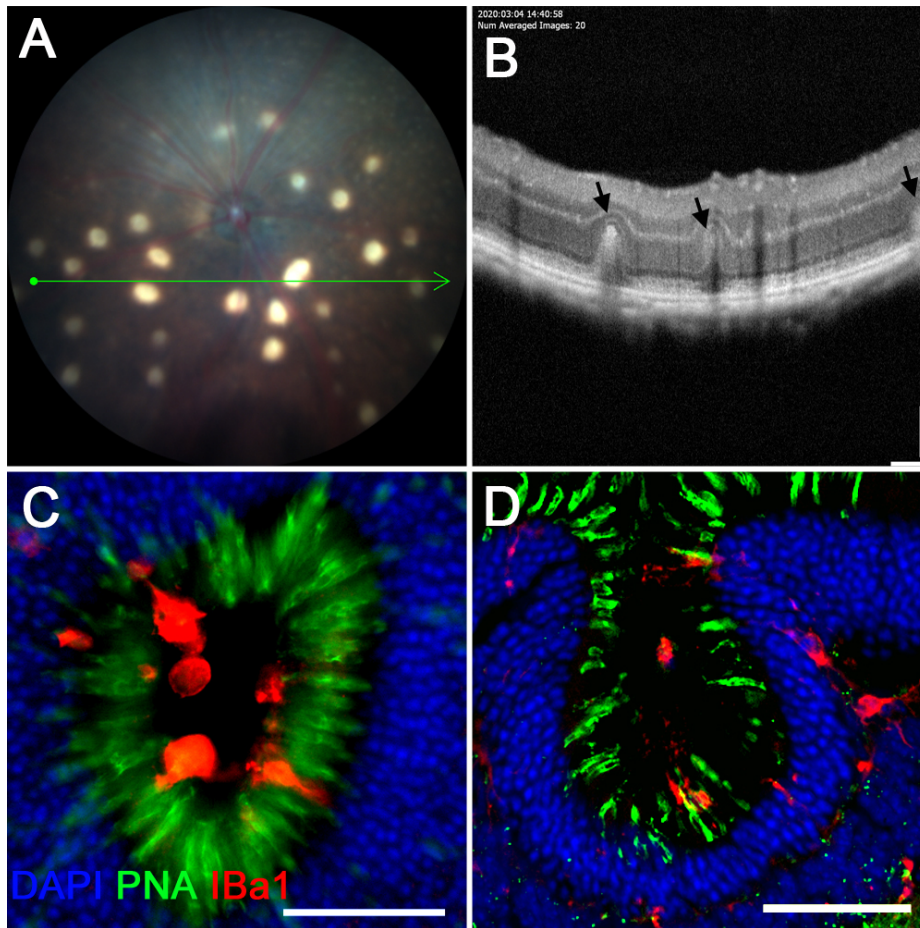
Figure S3. Retinal folds are often filled with microglia. (A-D) $^{rod}Tsc1^{-/-}$ mice at 4M of age. (A) Fundus image showing bright spots, which represent retinal folds and small white spots, which are microglia. (B) Image of OCT scan of eye shown in (A) along green arrow in (A). Three folds are visible (arrows) on OCT scan. (C) Zoomed in view on a retinal flat mount showing a fold filled with microglia (same panel as shown in Figure 3B). (D) Cross-section of a fold showing microglia inside and migrating from the inner nuclear layer towards the PR layer. (C, D: Blue: nuclear DAPI; green: peanut agglutinin lectin marking cone sheets; red: Iba-1 marking microglia).
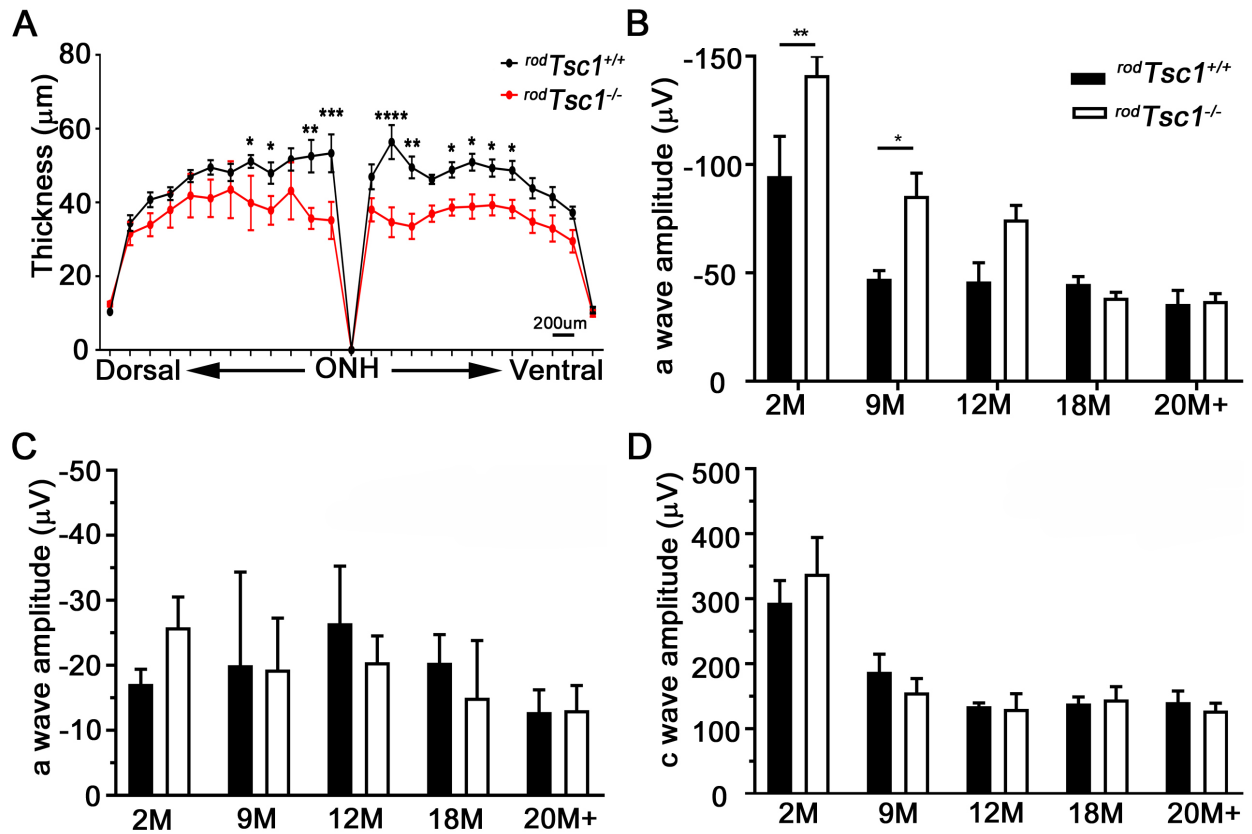
Figure S4. Loss of *Tsc1* in PRs does not lead to rapid PR degeneration. (A) Analysis of ONL thickness at 18M. Each symbol is mean ± S.E.M (n=6 retinas) (*p < 0.05; **p < 0.01; ***p < 0.0001). (B-D) Analyses of PRs function over time showing average a-wave amplitude of the scotopic (B) and photopic (C) responses and c-wave ERG amplitudes (D). Bars show mean ± S.E.M (n= 5, 5, 6, 4, 9 for *Cre⁻* and 8, 4, 4, 6, 5 for *Cre⁺* mice at 2M, 9M, 12M, 18M, and >20M respectively) (*p < 0.05; **p < 0.01).
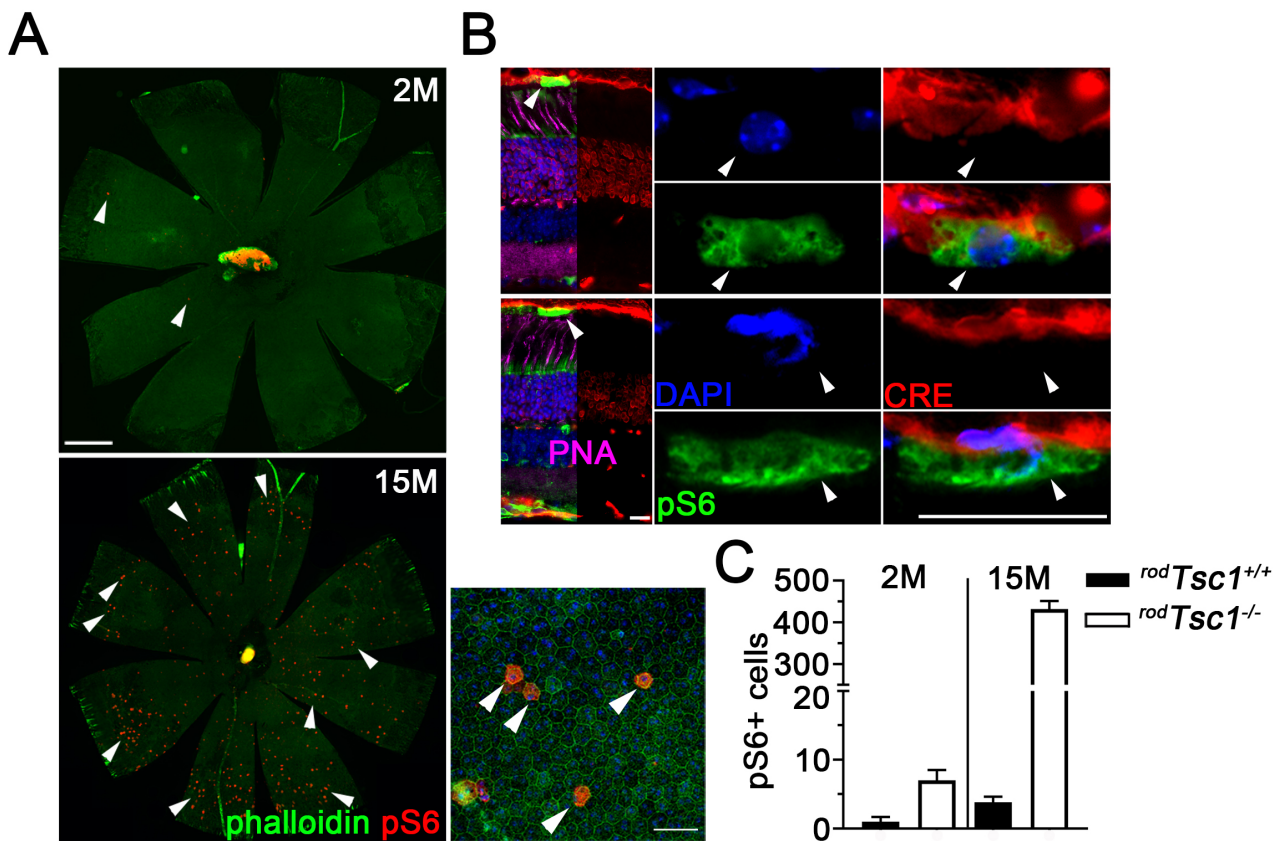
Figure S5. p-S6 in RPE cells is independent of CRE activity and increases over time. (A) Immunofluorescence for p-S6 (red signal) on RPE flat mounts of $^{rod}Tsc1^{-/-}$ mice at 2M (top) and 15M (bottom). Few p-S6 positive RPE cells (arrowheads) are seen at 2M. Bottom right shows higher magnification of pS6 positive RPE cells. Scale bar = 500 μm top panel on the left and 50 μm in bottom panel on the right. (Green: Phalloidin to highlight RPE cell boundaries). (B) Retinal sections showing CRE-Recombinase staining (red signal) in photoreceptor layer (left) but not in p-S6 positive (green signal) RPE cells (arrowhead; see enlarged images to the right). Two different examples are shown. Due to the strong signal of p-S6 in the RPE, signal intensity for p-S6 was reduced on cross-sections showing also retina. Thus p-S6 in PRs appears weaker than normal. Nuclear DAPI (blue signal) and peanut agglutinin lectin (magenta signal) were removed from 50% of panel to better visualize red and green signals. Scale bars = 20 μm. Red signal behind the RPE is due to the nature of the anti-CRE antibody, as it is a mouse monoclonal antibody highlighting therefore also endothelial cells. (C) Quantification of p-S6 positive RPE cells at 2M and 15M of genotypes indicated. Bars show mean ± S.E.M (n=4 mice).
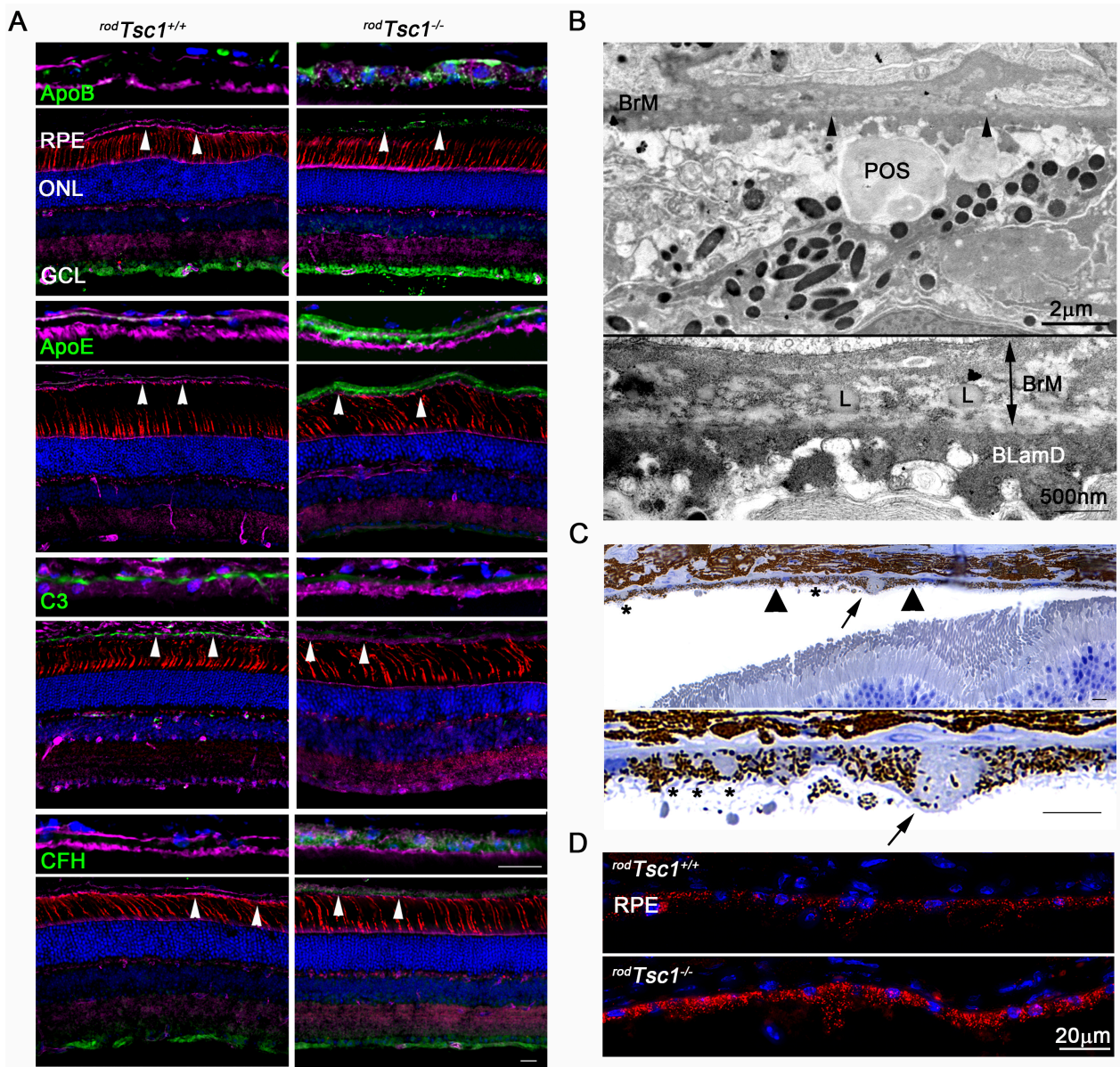
Figure S6. $^{rod}Tsc1^{-/-}$ **mice show early hallmarks of AMD.** (A) Immunofluorescence for ApoB, ApoE, C3 and CFH (green signal) on retinal sections of 15M old $^{rod}Tsc1^{-/-}$ mice. Higher magnification of the region between arrowheads is shown on top of each panel. (Blue: nuclear DAPI; red: cone sheets marked peanut agglutinin lectin (PNA); magenta: ZO-1 marking RPE boundaries for ApoE and C3 panels and Phalloidin marking boundaries for ApoB and CFH panels). Scale bar = 20 μm. Images are representatives of 3 independent experiments on 3 different animal per genotype. (B) Ultrastructural image showing undigested POS at the BrM, thickened BrM, neutral lipid droplets (L) in BrM and basal laminar deposit (BLamD). Enlarged image below shows area between arrowheads. (C) Semi-thin section showing basal mounds (asterisk) of different sizes (arrow: large basal mound). Higher magnification of region between arrowheads is shown below showing also micro-mounds (asterisks). Scale bar = 20 μm. (D) RPE autofluorescence of genotypes indicated at 15M. $^{rod}Tsc1^{-/-}$ mice show more accumulation of lipofuscin (red signal). Autofluorescence was acquired with a Cy3 filter. (Blue: nuclear DAPI). Scale bar = 20 μm.
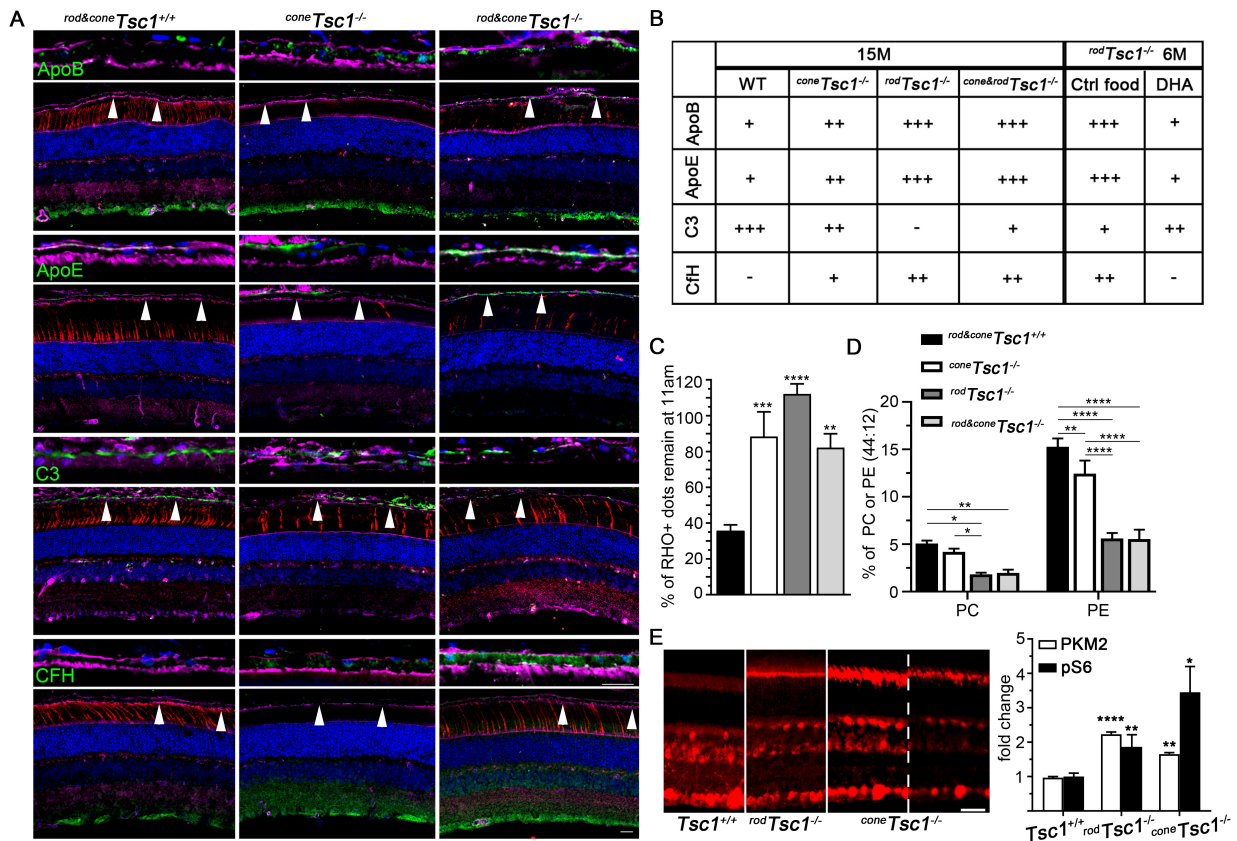
		15M				$^{rod}Tsc1^{-/-}$ 6M	
		WT	$^{cone}Tsc1^{-/-}$	$^{rod}Tsc1^{-/-}$	$^{cone\&rod}Tsc1^{-/-}$	Ctrl food	DHA
ApoB		+	++	+++	+++	+++	+
ApoE		+	++	+++	+++	+++	+
C3		+++	++	-	+	+	++
CfH		-	+	++	++	++	-

Figure S7. Similarities among $^{cone}Tsc1^{-/-}$ mice, $^{rod}Tsc1^{-/-}$ mice & $^{cone\&rod}Tsc1^{-/-}$ mice. (A) Immunofluorescence for ApoB, ApoE, C3 and CFH (green signal) on retinal sections of 15M old $^{cone\&rod}Tsc1^{+/+}$ control mice, $^{cone}Tsc1^{-/-}$ mice, and $^{cone\&rod}Tsc1^{-/-}$ mice. Higher magnification of the region between arrowheads is shown on top of each panel. (Blue: nuclear DAPI; red: peanut agglutinin lectin to detect cone segment; magenta: ZO1 to visualize RPE in ApoE and C3 panels or Phalloidin to visualize RPE in ApoB and CFH panels. Images are representative of 3 independent experiments with 3 different animals. Scale bars = 20 μm. (B) Summary of ApoB, ApoE, C3 and CFH expression changes seen in the different genotypes at 15M and in the DHA feeding experiment. Expression levels are indicated by "+" signs. Levels are arbitrary based on visual analyses of antibody staining in 3 animals per genotype. (C) POS clearance in genotypes indicated at 2M. Shown is the percentage of remaining dots at 11am. Loss of *Tsc1* in cones also affects digestion of rod outer segments as assays were performed with an anti-rhodopsin antibody. Bars show mean ± S.E.M. (n=6 RPE flat mounts). (D) Relative percentage of di-DHA PE (44:12) and PC (44:12) lipids from total retinal extracts of genotypes indicated at 2M. Bars show mean ± S.E.M. (n=8 for $^{cone\&rod}Tsc1^{+/+}$, n=6 for $^{rod}Tsc1^{-/-}$, n=5 for $^{cone}Tsc1^{-/-}$, n=3 for $^{cone\&rod}Tsc1^{-/-}$ with 2 retinas per sample from the same animal). (E) Immunofluorescence, as shown in Fig. 1B, for p-S6 (red signal) of genotypes indicated. Last two panels show $^{cone}Tsc1^{-/-}$ mice at same exposure (left panel of last two panels) and 75% reduced exposure (last panel). Signal in cones is much stronger than in rods thus the overall signal intensity needs to be reduced to see individual cells. The signal in the inner nuclear layer can be used as comparative reference. Scale bars: 50 μm. To the right, quantification of Western blots for p-S6 and PKM2 with retinas from 2M old mice (n=3) of genotypes indicated. Results are shown as mean ± S.E.M. (* P < 0.05**, P < 0.01, **** P < 0.0001).
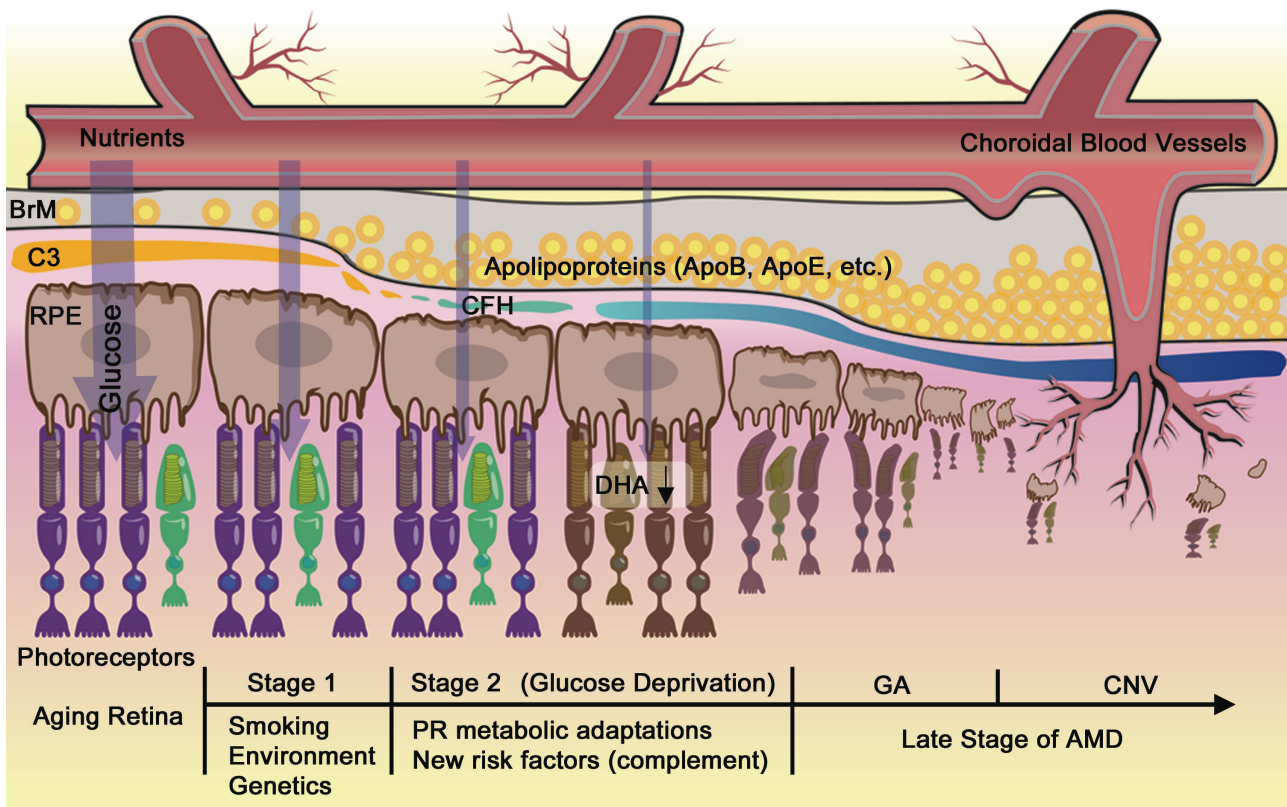
Figure S8. Schematic of two-stage disease progression. In the aging eye lipoproteins accumulate within the BrM (left side of image) as part of the normal aging process. In some individuals the accumulation of lipoproteins starts to exceed the normal age-related buildup resulting in the formation of a lipid wall (stage 1) at the RPE-BrM interphase. This stage is driven by environmental risk factors such as smoking, diet, lack of exercise and genetic risk factors that affect metabolism. Once the lipid barrier becomes too thick, glucose transfer from the choroidal vasculature to PRs is reduced. The reduction in glucose availability for photoreceptors results in metabolic adaptations in photoreceptors. These metabolic adaptations in PRs initiate the second stage of the disease. This leads to increased accumulation of lipoproteins, changes in the expression of complement components and a reduction of retinal di-DHA PE and PC lipids. The initiation of this disease stage adds also new risk alleles such as those of the complement and immune system. Eventually, in some individuals the pathologies progress to GA or choroidal neovascularization. The experiments shown in this study start with stage 2, meaning the initial lipid wall that forms during the first stage is missing in our experiments, which may explain why buildup of large drusen deposits is less pronounced. Our experiments also lack know risk factors that influence both proposed disease stages.